DOI:
10.1007/s10439-016-1625-3

Document Version
Peer reviewed version

Annals of Biomedical Engineering manuscript No.
(will be inserted by the editor)

A novel analytical approach to pulsatile blood flow in the arterial network

Joaquín Flores [1] · **Jordi Alastruey**[2] · **Eugenia Corvera Poiré**[1,3]

Received: date / Accepted: date

Abstract Haemodynamic simulations using one-dimensional (1-D) computational models exhibit many of the features of the systemic circulation under normal and diseased conditions. We propose a novel linear 1-D dynamical theory of blood flow in networks of flexible vessels that is based on a generalized Darcy's model and for which a full analytical solution exists in frequency domain. We assess the accuracy of this formulation in a series of benchmark test cases for which computational 1-D and 3-D solutions are available. Accordingly, we calculate blood flow and pressure waves, and velocity profiles in the human common carotid artery, upper thoracic aorta, aortic bifurcation, and a 20-artery model of the aorta and its larger branches. Our analytical solution is in good agreement with the available solutions and reproduces the main features of pulse waveforms in networks of large arteries under normal physiological conditions. Our model reduces computational time and provides a new approach for studying arterial pulse wave mechanics; *e.g.*

[1]Departamento de Física y Química Teórica, Facultad de Química, Universidad Nacional Autónoma de México, Ciudad Universitaria, México D.F. 04510, Mexico.
[2]Division of Imaging Sciences and Biomedical Engineering, St. Thomas' Hospital, King's College London, London, SE1 7EH, UK
[3] Departament de Física Fonamental, Universitat de Barcelona, Diagonal 647, E-08028 Barcelona, Spain
Address correspondence to E. Corvera Poiré, Departamento de Física y Química Teórica, Facultad de Química, Universidad Nacional Autónoma de México, Ciudad Universitaria, México D.F. 04510, Mexico.
Electronic mails: eugenia.corvera@gmail.com; jordi.alastruey-arimon@kcl.ac.uk; joaquin.flores.iq@gmail.com

the analyticity of our model allows for a direct identification of the role played by physical properties of the cardiovascular system on the pressure waves.

Keywords 1-D arterial haemodynamics; pulse wave propagation; 1-D blood flow modelling; generalized Darcy's model; benchmark test cases;

1 Introduction

Pulsatile blood flow in the systemic arterial tree is generated by the contraction of the left ventricle (LV). The pulse wave propagates in the arterial tree distending and contracting blood vessels (*e.g.* it produces the pulse that can be felt in the wrist) and producing changes in blood pressure and flow in time and space. These changes are determined by physical properties of the cardiovascular system, some of which are altered by disease; *e.g.* heart contraction, arterial stiffness, and peripheral vascular resistance. Therefore, the shapes of pressure and flow contours (also called pulse waves) measured at a given arterial site carry valuable information about the functionality of the cardiovascular system. However, it is not clear yet what is the relative role of physical properties of the heart, large arteries and smaller blood vessels in generating arterial pulse waves in normal conditions or with diseases such as hypertension.

Different modelling approaches have been proposed to study arterial blood flow. Lumped parameter zero-dimensional (0-D) models, group the properties of the cardiovascular system without considering its spatial characteristics. They are described by ordinary differential equations and, hence, provide a computationally inexpensive and mathematically simple framework to study whole-system dynamics.[13,21,46,50,52] However, they are not suitable for studying pulse wave propagation phenomena. 0-D accumulated and one-dimensional (1-D) models can accurately describe pulsatile blood flow in the arterial network while keeping the computational cost down.[1,4,6,7,20,27,29,32,33,35,40,41,47,53] Three-dimensional (3-D) techniques are used to describe complex 3-D flow features and their interaction with the vessel wall, such as those observed in stenosis and aneurysms.[9,17,23,24,37,38,45,48]

On the downside, using 3-D techniques to investigate arterial pulse wave propagation is computationally expensive.

Lumped parameter 0-D models relate the blood pressure and flow waveforms with global properties of the cardiovascular system, such as arterial compliance, peripheral vascular resistance and outflow pressures. They provide clinically useful analytical relations between global cardiovascular properties (*e.g.* peripheral vascular resistance and arterial compliance) and blood pressure in conditions such as hypertension.[52] Analytical solutions for 1-D pulse wave propagation phenomena have been proposed for a single vessel[25,36] and have been used as boundary conditions representing downstream vessels in 1-D[35] or 3-D[51] formulations. However, we are unaware of any analytical 1-D models of blood flow in networks containing the aorta and larger systemic branches. Such a model could allow us to quickly investigate the role of individual physical properties of the cardiovascular system on pulse waveforms. This is important, for instance, to identify properties responsible for pathological conditions – *e.g.* changes in the pressure waveform with hypertension – that should be targeted for improved treatment.

The aim of this paper is to present and validate a novel linear 1-D formulation of blood flow in networks of flexible vessels for which a full analytical solution exists in frequency domain. We call it the generalized Darcy's elastic model (GDEM) since it is based on a 0-D generalized Darcy's model (GDM) for pulsatile flow in rigid vessels,[12,14,15] which was previously extended to study flow in tree-like networks of rigid vessels.[19] The GDM has been used to analyze numerically and analytically the effects that different anatomical variations (anastomosis, obstructions, vessel suppression) have on the total flow through a network.[18,49]

We first introduce the governing equations of the GDEM and their analytical solution to describe blood flow in a single elastic vessel and in a network of elastic vessels. We assess the accuracy of this formulation in a series of benchmark test cases for which computational 1-D and 3-D solutions are available from Xiao *et al.*[55] These tests show the ability of the analytical GDEM to reproduce the main

features of pulse waves and velocity profiles. We finish with a section of Discussion in which Conclusions and Perspectives are comprised.

2 Materials and Methods

We introduce the governing equations of our novel GDEM model for blood flow in a network of elastic vessels. The network is decomposed into segments connected to each other at nodes. Each segment is modeled as a deformable tube, representing a blood vessel. We present the theory, first for a single vessel, and then for a generic network. Further details on the derivation of the GDEM model are given in Appendix I.

2.1 Generalized Darcy's Elastic Model (GDEM) for a single vessel

By assuming the vessel wall to have a cylindrical shape; the wall to be impermeable; blood to be a Newtonian or a Maxwellian fluid, of density ρ and viscosity η; and no-slip boundary conditions for the axial velocity at the average wall position, R_0, conservation of momentum in frequency domain gives an expression for the local axial velocity of the fluid, $\hat{u}(x, r, \omega)$, that is linearly related to the pressure gradient along the flow direction:

$$\hat{u} = -\frac{K_L(r,\omega)}{\eta}\ \frac{\partial \hat{p}}{\partial x}, \tag{1}$$

where x and r are the axial and radial coordinates, and $K_L(r, \omega)$ is a local dynamic permeability, given by:

$$K_L(r,\omega) = -\frac{\eta}{i\omega\rho}\left[1 - \frac{J_0(kr)}{J_0(kR_0)}\right]. \tag{2}$$

Here $k^2 = \frac{\rho}{\eta}\left(t_r\omega^2 + i\omega\right)$, where t_r is the fluid relaxation time (zero when blood is assumed to be Newtonian, finite when it is Maxwellian), and $i = \sqrt{-1}$. The hat

in pressure and velocity, indicates that they are in frequency domain; *i.e.* they are functions of space and frequency.

Averaging Eq. (1) over the average cross-sectional area, A_0, gives an expression for the flow in frequency domain, $\hat{Q}$, across A_0, which is called a generalized Darcy's law in frequency domain and is given by

$$\hat{Q} = -\frac{A_0 K(\omega)}{\eta} \frac{\partial \hat{p}}{\partial x}. \tag{3}$$

Here $K(\omega)$ is the dynamic permeability:

$$K(\omega) = -\frac{\eta}{i\omega\rho}\left[1 - \frac{2J_1(kR_0)}{kR_0 J_0(kR_0)}\right]. \tag{4}$$

Equations (1) and (3) were originally derived for a constant pressure gradient along the flow direction.[14,25] However, in this work we assume that they are valid locally; *i.e.* , that at any position x, the local pressure gradient determines both the local velocity and the flow, and that their x-dependence comes solely from the pressure gradient. Both, $K_L(\omega)$ and $K(\omega)$ are measurements of the resistance to blood flow.

By assuming the vessel wall to be a linear elastic tube that follows Hooke's law, an expression relating changes in pressure with changes in the luminal cross-sectional area can be obtained (see Appendix I). This can be coupled to the axial velocity by conservation of mass to give

$$-i\omega C\hat{p} + \frac{\partial \hat{Q}}{\partial x} = 0, \tag{5}$$

which relates pressure, $\hat{p}(x,\omega)$, and the flow, $\hat{Q}(x,\omega)$, in the frequency domain. The constant C is called the vessel compliance, and is given by

$$C = \frac{3\pi R_0 R_{\mathrm{d}}^2}{2Eh}, \tag{6}$$

where E is the Young modulus, h is the vessel thickness, and $R_{\rm d}$ is the radius at diastole.

2.1.1 Solution for pressure, flow and velocity profiles in frequency domain

We show how to calculate blood flow and pressure in the frequency domain as a function of the axial coordinate. Differentiation of Eq. (3) with respect to x and substitution into Eq. (5) yields the following harmonic oscillator equation for pressure in frequency domain,

$$\left(\frac{\partial^2 \hat{p}}{\partial x^2}\right) = -k_c^2 \hat{p}, \tag{7}$$

with a complex constant $k_c^2 = \dfrac{i\omega C\eta}{A_0 K(\omega)}$. The solution of Eq. (7) subject to the boundary conditions $\hat{p}(x=0,\omega) = \hat{p}_{\rm in}$, for the pressure at the inlet ($x=0$), and $\hat{p}(x=l,\omega) = \hat{p}_o$, for the pressure at the outlet ($x=l$), is given by:

$$\hat{p}(x) = \hat{p}_{\rm in}\cos(k_c x) + \frac{\hat{p}_{\rm o} - \hat{p}_{\rm in}\cos(k_c l)}{\sin(k_c l)}\sin(k_c x). \tag{8}$$

Differentiation of Eq. (8) with respect to x gives the pressure gradient as a function of the axial position in an elastic tube; *i.e.*

$$\frac{\partial \hat{p}}{\partial x} = -k_c\ \hat{p}_{\rm in}\sin\left(k_c x\right) + k_c\frac{\hat{p}_{\rm o} - \hat{p}_{\rm in}\cos\left(k_c l\right)}{\sin\left(k_c l\right)}\cos\left(k_c x\right). \tag{9}$$

It should be noted that the elasticity of the vessel determines the variation of the pressure gradient along the vessel, Eq. (9), while the generalized Darcy's law for a rigid tube, Eq. (3), gives the flow along the axial direction since Eq. (3) is considered to be locally valid for any pressure gradient.

As a result, substitution of Eq. (9) into (3) yields the flow along the axial direction for an elastic tube:

$$\hat{Q}(x) = M\left(\hat{p}_{\rm in}\sin\left(k_c x\right) - \frac{\hat{p}_o - \hat{p}_{\rm in}\cos\left(k_c l\right)}{\sin\left(k_c l\right)}\cos\left(k_c x\right)\right), \tag{10}$$

where

$$M^2 = \frac{i\omega C A_0 K(\omega)}{\eta}. \tag{11}$$

Similarly, substitution of Eq. (9) into the local Darcy's law for a rigid tube, Eq. (1), gives the velocity profiles along the flow direction:

$$\hat{u}(r,x) = M_L(r)\left(\hat{p}_{\text{in}}\sin\left(k_c x\right) - \frac{\hat{p}_o - \hat{p}_{\text{in}}\cos\left(k_c l\right)}{\sin\left(k_c l\right)}\cos\left(k_c x\right)\right), \tag{12}$$

where

$$M_L(r) = \frac{M}{A_0 K(\omega)} K_L(r,\omega). \tag{13}$$

Equations (8), (10) and (12) enable calculation of the pressure, flow and velocity profile at any position along a vessel as a function of the pressures in its extremes.

2.1.2 Pressure, flow and velocity profiles for vessels with different type of connections within a network

A generic network of vessels may have multiple inputs and outputs. In this study we impose volume flow rates at the input boundary conditions and couple three-element Windkessel models at the outputs to obtain a system of equations for the pressures at the network internal nodes (presented in the next section). Vessels can be classified into the following three types (see Fig. 1), depending on their boundary conditions:

– Vessel Type I (see Fig. 1a). This has an inflow as boundary condition and a pressure $\hat{p}_{\text{o}}$ at the outlet, which is to be determined as part of the solution. Once $\hat{p}_{\text{o}}$ is known, the pressure, flow and velocity profiles along the vessel are given by:

$$\hat{p}(x) = \frac{\hat{Q}_{\text{in}}\sin(k_c l) + M\hat{p}_{\text{o}}}{M\cos(k_c l)}\cos(k_c x) - \frac{\hat{Q}_{\text{in}}}{M}\sin(k_c x), \tag{14}$$

$$\hat{Q}(x) = \frac{\hat{Q}_{\text{in}}\sin(k_c l) + M\hat{p}_{\text{o}}}{\cos(k_c l)}\sin(k_c x) + \hat{Q}_{\text{in}}\cos(k_c x), \tag{15}$$

$$\hat{u}(r,x) = \frac{M_L(r)}{M}\left(\frac{\hat{Q}_{\text{in}}\sin(k_c l) + M\hat{p}_{\text{o}}}{\cos(k_c l)}\sin(k_c x) + \hat{Q}_{\text{in}}\cos(k_c x)\right). \tag{16}$$

Equation (14) is obtained from Eq. (10) evaluated at $x = 0$ and Eq. (8). Equations (15) and (16) are obtained by differentiating Eq. (14) and substituting the result into Eqs. (3) and (1), respectively.

– Vessel Type II (see Fig. 1b). This has pressures – to be determined as part of the solution – both at the inlet, $\hat{p}_{\text{in}}$, and outlet, $\hat{p}_{\text{o}}$. Once these are known, pressure, flow and velocity profiles along the vessel are given by Eqs. (8), (10), and (12).

– Vessel Type III (see Fig. 1c). This has a pressure at the inlet, $\hat{p}_{\text{in}}$, and a Windkessel boundary condition coupled to the pressure, $\hat{p}_{\text{o}}$, at the vessel outlet. Both $\hat{p}_{\text{in}}$ and $\hat{p}_{\text{o}}$ are to be determined as part of the solution. Once they are known, flow and pressure along the vessel are given by Eqs. (8) and (10). Each Windkessel model relates the pressure and the flow at the end point of a terminal vessel through

$$Q_{\text{Wk}}\left(1 + \frac{R_1}{R_2}\right) + C_{\text{Wk}}R_1\frac{\partial Q_{\text{Wk}}}{\partial t} = \frac{p_0 - p_{\text{out}}}{R_2} + C_{\text{Wk}}\frac{\partial p_0}{\partial t}. \tag{17}$$

It consists of a resistance R_1 connected in series with a parallel combination of a second resistance R_2 and a compliance C_{Wk}. The resistance R_1 is equal to the characteristic impedance of the end point in the terminal vessel in order to minimize wave reflections.[3] Equation (17) in frequency domain is given by

$$\hat{Q}_{\text{Wk}} = \frac{\hat{p}_0}{\hat{Z}}, \tag{18}$$

where the impedance $\hat{Z}$ is

$$\hat{Z} = \frac{R_1 + R_2 - i\omega R_1 R_2 C_{\text{Wk}}}{1 - i\omega R_2 C_{\text{Wk}}}. \tag{19}$$

2.2 Generalized Darcy's Elastic Model for a network of vessels

Here we show how to write a system of equations for the pressures in the nodes as a function of known blood and vessel properties, and boundary conditions for inflows and Windkessel terminal branches. We define a node as the mathematical point where two or three vessels are connected. Nodes can be classified into the following four types depending on the type of vessels that they connect (see Fig. 2). Hereafter, superscripts will denote the vessel number for the flows, and superscript in squared brackets will denote the node number for pressures.

– Node Type I (see Node N in Fig. 2). This has an unknown pressure $p^{[N]}$ and connects one vessel of Type I (h) and two vessels Type II ($h+1$ and $h+2$). At node N, flow conservation can be expressed as

$$\hat{Q}_{\mathrm{o}}^{h} = \hat{Q}_{\mathrm{in}}^{h+1} + \hat{Q}_{\mathrm{in}}^{h+2}, \tag{20}$$

where the outflow $\hat{Q}_{\mathrm{o}}^{h}$ is obtained from Eq. (15) evaluated at $x = l$ and the inflows $\hat{Q}_{\mathrm{in}}^{h+1}$ and $\hat{Q}_{\mathrm{in}}^{h+2}$ are given by Eq. (10) evaluated at $x = 0$. This gives

$$\frac{\hat{Q}_{\mathrm{in}}^{h} + M^{h}\hat{p}^{[N]}\sin(k_c^h l^h)}{\cos(k_c^h l^h)} =$$

$$-M^{h+1}\left(\frac{\hat{p}^{[N+1]} - \hat{p}^{[N]}\cos(k_c^{h+1}l^{h+1})}{\sin(k_c^{h+1}l^{h+1})}\right) - M^{h+2}\left(\frac{\hat{p}^{[N+2]} - \hat{p}^{[N]}\cos(k_c^{h+2}l^{h+2})}{\sin(k_c^{h+2}l^{h+2})}\right). \tag{21}$$

– Node Type II (see Node S in Fig. 2). This has an unknown pressure $p^{[S]}$ and connects three vessels of Type II: j, $j+1$ and $j+2$. At node S, flow conservation is expressed as

$$\hat{Q}_{\mathrm{o}}^{j} = \hat{Q}_{\mathrm{in}}^{j+1} + \hat{Q}_{\mathrm{in}}^{j+2}. \tag{22}$$

For the outflow of vessel j, we evaluate Eq. (10) at $x = l$; for the inflows $\hat{Q}_{\mathrm{in}}^{j+1}$ and $\hat{Q}_{\mathrm{in}}^{j+2}$, we evaluate Eq. (10) at $x = 0$. Thus, we can write flow conservation

as

$$M^j\left(\frac{\hat{p}^{[S-1]}-\hat{p}^{[S]}\cos(k_c^j l^j)}{\sin(k_c^j l^j)}\right)=$$

$$-M^{j+1}\left(\frac{\hat{p}^{[S+1]}-\hat{p}^{[S]}\cos(k_c^{j+1} l^{j+1})}{\sin(k_c^{j+1} l^{j+1})}\right)-M^{j+2}\left(\frac{\hat{p}^{[S+2]}-\hat{p}^{[S]}\cos(k_c^{j+2} l^{j+2})}{\sin(k_c^{j+2} l^{j+2})}\right). \tag{23}$$

– Node Type III (see Node $T-1$ in Fig. 2). This has an unknown pressure $p^{[T-1]}$ and connects two vessels of Type II: $m-1$ and m. At node $T-1$ flow conservation is expressed as

$$\hat{Q}_{\mathrm{o}}^{m-1}=\hat{Q}_{\mathrm{in}}^{m}. \tag{24}$$

For the outflow of vessel $m-1$, we evaluate Eq. (10) at $x=l$ and for the inflow of vessel m, we evaluate Eq. (10) at $x=0$, so that we can write flow conservation as

$$M^{m-1}\left(\frac{\hat{p}^{[T-2]}-\hat{p}^{[T-1]}\cos(k_c^{m-1} l^{m-1})}{\sin(k_c^{m-1} l^{m-1})}\right)=-M^{m}\left(\frac{\hat{p}^{[T]}-\hat{p}^{[T-1]}\cos(k_c^{m} l^{m})}{\sin(k_c^{m} l^{m})}\right). \tag{25}$$

– Node Type IV (see Node T in Fig. 2). This has an unknown pressure $p^{[T]}$ and is the node that connects the terminal vessel m of Type III, with the three-element Windkessel model. At node T, flow conservation is given by

$$\hat{Q}_{\mathrm{o}}^{m}=\hat{Q}_{\mathrm{Wk}}^{m}. \tag{26}$$

To obtain $\hat{Q}_{\mathrm{o}}^{m}$, we evaluate Eq. (10) at $x=l$. For the Windkessel flow connected to vessel m, $\hat{Q}_{\mathrm{Wk}}^{m}$, we use Eq. (18). Thus, we can write the flow conservation equation as

$$M^{m}\left(\frac{\hat{p}^{[T-1]}-\hat{p}^{[T]}\cos(k_c^{m} l^{m})}{\sin(k_c^{m} l^{m})}\right)=\frac{\hat{p}^{[T]}}{\hat{Z}^{m}}. \tag{27}$$

Our formulation gives a system of equations for the pressures at the nodes. To shorten the notation in matrix form, we define three quantities, κ_1, κ_2 and κ_3,

that depend upon the characteristics of a single vessel, the properties of the fluid, and frequency:

$$\kappa_1^i \equiv M^i \frac{\cos(k_c^i l^i)}{\sin(k_c^i l^i)}, \qquad \kappa_2^i \equiv M^i \frac{1}{\sin(k_c^i l^i)}, \qquad \text{and} \qquad \kappa_3^i \equiv M^i \frac{\sin(k_c^i l^i)}{\cos(k_c^i l^i)}, \quad (28)$$

where the superscript i denotes the vessel number and M is given by Eq. (11). In terms of these quantities, Eqs. (21), (23), (25) and (27) for node Types I, II, III and IV, can be written respectively as:

$$\left(\kappa_3^h - \kappa_1^{h+1} - \kappa_1^{h+2}\right)\hat{p}^{[N]} + \kappa_2^{h+1}\hat{p}^{[N+1]} + \kappa_2^{h+2}\hat{p}^{[N+2]} = -\frac{\hat{Q}_{\text{in}}^h}{\cos(k_c^h l^h)} \ , \quad (29)$$

$$\kappa_2^j\ \hat{p}^{[S-1]} - \left(\kappa_1^j + \kappa_1^{j+1} + \kappa_1^{j+2}\right)\hat{p}^{[S]} + \kappa_2^{j+1}\hat{p}^{[S+1]} + \kappa_2^{j+2}\hat{p}^{[S+2]} = 0 \ , \quad (30)$$

$$\kappa_2^{m-1}\hat{p}^{[T-2]} - \left(\kappa_1^{m-1} + \kappa_1^m\right)\hat{p}^{[T-1]} + \kappa_2^m\ \hat{p}^{[T]} = 0 \ , \quad (31)$$

$$\kappa_2^m\ \hat{p}^{[T-1]} - \left(\kappa_1^m + \frac{1}{Z^m}\right)\hat{p}^{[T]} = 0 \ . \quad (32)$$

The system in matrix form is given by $\mathbf{K}\hat{\mathbf{p}} = \hat{\mathbf{Q}}$, where the matrix $\mathbf{K}$ that explicitly contains the terms for each of the four types of nodes is given by:

$$\mathbf{K} = \begin{pmatrix}
\kappa_3^h - \kappa_1^{h+1} - \kappa_1^{h+2} & \kappa_2^{h+1} & \kappa_2^{h+2} & \cdots & 0 & 0 & 0 & 0 & \cdots & 0 & 0 & 0 & \cdots \\
\vdots & \vdots & \vdots & \vdots & \vdots & \vdots & \vdots & \vdots & \vdots & \vdots & \vdots & \vdots & \vdots \\
0 & 0 & 0 & \cdots & \kappa_2^j & -\kappa_1^j - \kappa_1^{j+1} - \kappa_1^{j+2} & \kappa_2^{j+1} & \kappa_2^{j+2} & \cdots & 0 & 0 & 0 & \cdots \\
\vdots & \vdots & \vdots & \vdots & \vdots & \vdots & \vdots & \vdots & \vdots & \vdots & \vdots & \vdots & \vdots \\
0 & 0 & 0 & \cdots & 0 & 0 & 0 & 0 & \cdots & \kappa_2^{m-1} & -\kappa_1^{m-1} - \kappa_1^m & \kappa_2^m & \cdots \\
0 & 0 & 0 & \cdots & 0 & 0 & 0 & 0 & \cdots & 0 & \kappa_2^m & -\kappa_1^m - \frac{1}{Z^m} & \cdots \\
\vdots & \vdots & \vdots & \vdots & \vdots & \vdots & \vdots & \vdots & \vdots & \vdots & \vdots & \vdots & \ddots
\end{pmatrix},$$

$$\hat{\mathbf{p}} = \begin{pmatrix} \hat{p}^{[N]} \\ \hat{p}^{[N+1]} \\ \hat{p}^{[N+2]} \\ \vdots \\ \hat{p}^{[S-1]} \\ \hat{p}^{[S]} \\ \hat{p}^{[S+1]} \\ \hat{p}^{[S+2]} \\ \vdots \\ \hat{p}^{[T-2]} \\ \hat{p}^{[T-1]} \\ \hat{p}^{[T]} \\ \vdots \end{pmatrix} \quad \text{and} \quad \hat{\mathbf{Q}} = \begin{pmatrix} -\frac{\hat{Q}^h_{in}}{\cos(k^h_c l^h)} \\ \vdots \\ 0 \\ \vdots \\ 0 \\ 0 \\ \vdots \end{pmatrix}.$$

The solution for the pressures at the nodes, $\hat{\mathbf{p}}$, is given by the product of the inverse matrix, $\mathbf{K^{-1}}$, and the vector of the inflow boundary conditions, $\hat{\mathbf{Q}}$; *i.e.* $\hat{\mathbf{p}} = \mathbf{K^{-1}}\hat{\mathbf{Q}}$. The matrix $\mathbf{K}$, and its inverse $\mathbf{K^{-1}}$, contain the characteristics of the vessels, the properties of the fluid, and the Windkessel boundary conditions. They can be considered to be response functions of the several-inputs, several-outputs system. $\mathbf{K^{-1}}$ can be obtained by inverting symbolically the matrix $\mathbf{K}$. Once the pressures at the nodes are known, Eqs. (8), (10), and (12) can be used to obtain analytically the pressure, flow and velocity profiles in frequency domain along any vessel in the network.

2.2.1 Coupling of time-domain boundary conditions with the frequency-domain analytical formulation

In vivo measurements are always obtained in time-domain. Our formulation is done in frequency domain except that we have to Fourier transform in-vivo inputs to Fourier domain to use them as boundary conditions and anti-transforme pressure, flow and velocity profiles results to time domain in order to relate them with signals that can be compared with measured quantities and interpreted physically.

The transformation from time to frequency domain and the inverse transformation from frequency to time domain have to be done numerically.

2.2.2 Solutions for Particular Models

Single vessel model

A single-vessel model involves a combination of vessel Types I and III, since we have as boundary conditions the inflow, in one extreme, and the three-element Windkessel model in the other (Fig. 3). At the outlet of the vessel, flow conservation yields

$$\hat{Q}_{\mathrm{o}} = \hat{Q}_{\mathrm{Wk}}, \tag{33}$$

where the outflow of the vessel, $\hat{Q}_{\mathrm{o}}$, is given by Eq. (15) evaluated at $x = l$, and the flow in the Windkessel model, $\hat{Q}_{\mathrm{Wk}}$, is given by Eq. (18). This allows to rewrite Eq. (33) as

$$\frac{\hat{Q}_{\mathrm{in}} + M\hat{p}_{\mathrm{o}}\sin(k_c l)}{\cos(k_c l)} = \frac{\hat{p}_{\mathrm{o}}}{\hat{Z}}, \tag{34}$$

where $\hat{Z}$ is given by Eq. (19). Since this is the simplest possible model, we have a 1 x 1 matrix describing the response of the system and vectors with only one element for the pressure and the inflow. Solving for the pressure $\hat{p}_{\mathrm{o}}$ we have

$$\hat{p}_{\mathrm{o}} = \frac{\hat{Z}\hat{Q}_{\mathrm{in}}}{\cos(k_c l) - \hat{Z}M\sin(k_c l)}. \tag{35}$$

Using this expression for $\hat{p}_{\mathrm{o}}$ into Eqs. (14), (15) and (16), we obtain the pressure, flow and velocity profiles, in frequency domain, as a function of the axial direction x,

$$\hat{p}(x) = \left[\frac{\sin(k_c l)\cos(k_c x)}{\cos(k_c l)} - \sin(k_c x)\right]\frac{\hat{Q}_{\mathrm{in}}}{M} + \left[\frac{\cos(k_c x)}{\cos(k_c l)\left(\cos(k_c l) - \hat{Z}M\sin(k_c l)\right)}\right]\hat{Q}_{\mathrm{in}}\hat{Z}, \tag{36}$$

$$\hat{Q}(x) = \left[\frac{\sin(k_c l)\sin(k_c x)}{\cos(k_c l)} + \cos(k_c x)\right]\hat{Q}_{\mathrm{in}} + \left[\frac{\sin(k_c x)}{\cos(k_c l)\left(\cos(k_c l) - \hat{Z}M\sin(k_c l)\right)}\right]\hat{Q}_{\mathrm{in}}M\hat{Z}, \tag{37}$$

$$\hat{u}(r,x)=\left[\frac{\sin(k_c l)\sin(k_c x)}{\cos(k_c l)}+\cos(k_c x)\right]\frac{M_L(r)\hat{Q}_{\rm in}}{M}+\left[\frac{\sin(k_c x)}{\cos(k_c l)\left(\cos(k_c l)-\hat{Z}M\sin(k_c l)\right)}\right]\hat{Q}_{\rm in}M_L(r)\hat{Z}. \tag{38}$$

Single bifurcation model

We consider a model for a bifurcation, containing a parent segment, and two branch segments. In order to obtain the system of equations for the pressures in the nodes, we use the notation of Fig. 4. Node 1 is of Type I and Nodes 2 and 3 are of Type IV. Thus, following Eqs.(29) and (32), the system of equations for the pressures at the nodes, in matrix form, is given by:

$$\begin{pmatrix} \kappa_3^1-\kappa_1^2-\kappa_1^3 & \kappa_2^2 & \kappa_2^3 \\ \kappa_2^2 & -\kappa_1^2-\frac{1}{\hat{Z}^2} & 0 \\ \kappa_2^3 & 0 & -\kappa_1^3-\frac{1}{\hat{Z}^3} \end{pmatrix}\begin{pmatrix} \hat{p}^{[1]} \\ \hat{p}^{[2]} \\ \hat{p}^{[3]} \end{pmatrix}=\begin{pmatrix} -\frac{Q_{\rm in}^1}{\cos(k_c^1 l^1)} \\ 0 \\ 0 \end{pmatrix}.$$

By inverting symbolically the matrix we can obtain the following analytical expressions for the pressures at the nodes:

$$\hat{p}^{[1]}=-\frac{\hat{Q}_{\rm in}^1\left(1+\kappa_1^2\hat{Z}^2+\kappa_1^3\hat{Z}^3+\kappa_1^2\kappa_1^3\hat{Z}^2\hat{Z}^3\right)}{\cos(k_c^1 l^1)\left[\hat{Z}^3(1+\hat{Z}^2\kappa_1^2)(\kappa_2^3)^2-(1+\hat{Z}^3\kappa_1^3)\left(\kappa_1^2+\kappa_1^3-\kappa_3^1+\hat{Z}^2\left[(\kappa_1^2)^2+\kappa_1^2\kappa_1^3-\kappa_1^2\kappa_3^1-(\kappa_2^2)^2\right]\right)\right]}, \tag{39}$$

$$\hat{p}^{[2]}=-\frac{\hat{Q}_{\rm in}^1\left(\kappa_2^2\hat{Z}^2+\kappa_2^2\kappa_1^3\hat{Z}^2\hat{Z}^3\right)}{\cos(k_c^1 l^1)\left[\hat{Z}^3(1+\hat{Z}^2\kappa_1^2)(\kappa_2^3)^2-(1+\hat{Z}^3\kappa_1^3)\left(\kappa_1^2+\kappa_1^3-\kappa_3^1+\hat{Z}^2\left[(\kappa_1^2)^2+\kappa_1^2\kappa_1^3-\kappa_1^2\kappa_3^1-(\kappa_2^2)^2\right]\right)\right]}, \tag{40}$$

$$\hat{p}^{[3]}=-\frac{\hat{Q}_{\rm in}^1\left(\kappa_2^3\hat{Z}^3+\kappa_1^2\kappa_2^3\hat{Z}^2\hat{Z}^3\right)}{\cos(k_c^1 l^1)\left[\hat{Z}^3(1+\hat{Z}^2\kappa_1^2)(\kappa_2^3)^2-(1+\hat{Z}^3\kappa_1^3)\left(\kappa_1^2+\kappa_1^3-\kappa_3^1+\hat{Z}^2\left[(\kappa_1^2)^2+\kappa_1^2\kappa_1^3-\kappa_1^2\kappa_3^1-(\kappa_2^2)^2\right]\right)\right]}. \tag{41}$$

Equation (39) can be used as the output pressure in Eqs. (14), (15), and (16), in order to obtain the pressure, the flow, and the velocity profiles in the parent vessel. Equations (39), (40) and (41) can be used in Eqs. (8), (10), and (12) in order to obtain the pressure, the flow, and the velocity profiles, along the two daughter vessels. For the particular case in which they are identical, $\kappa_1^2=\kappa_1^3$, $\kappa_2^2=\kappa_2^3$, and the characteristic impedances $\hat{Z}^2=\hat{Z}^3$. As a result, $\hat{p}_2(x)=\hat{p}_3(x)$ and $\hat{Q}_2(x)=\hat{Q}_3(x)$. Equations for pressures, flows, and velocity profiles, along the

parent and daughter vessels reduce to:

$$\hat{p}_1(x) = -\frac{\hat{Q}^1_{\text{in}}\left(1+\hat{Z}^2\kappa_1^2\right)\cos(k_c^1 x)}{\cos^2(k_c^1 l^1)\left[\kappa_3^1 - 2\kappa_1^2 + \hat{Z}^2\left(\kappa_1^2\kappa_3^1 - 2(\kappa_1^2)^2 + 2(\kappa_2^2)^2\right)\right]} + \frac{\hat{Q}^1_{\text{in}}\sin(k_c^1 l^1)}{M^1\cos(k_c^1 l^1)}\cos(k_c^1 x) - \frac{\hat{Q}^1_{\text{in}}}{M^1}\sin(k_c^1 x), \tag{42}$$

$$\hat{Q}_1(x) = -\frac{M^1\hat{Q}^1_{\text{in}}\left(1+\hat{Z}^2\kappa_1^2\right)\sin(k_c^1 x)}{\cos^2(k_c^1 l^1)\left[\kappa_3^1 - 2\kappa_1^2 + \hat{Z}^2\left(\kappa_1^2\kappa_3^1 - 2(\kappa_1^2)^2 + 2(\kappa_2^2)^2\right)\right]} + \frac{\hat{Q}^1_{\text{in}}\sin(k_c^1 l^1)}{\cos(k_c^1 l^1)}\sin(k_c^1 x) + \hat{Q}^1_{\text{in}}\cos(k_c^1 x), \tag{43}$$

$$\hat{u}_1(r,x) = -\frac{M_L(r)^1\hat{Q}^1_{\text{in}}\left(1+\hat{Z}^2\kappa_1^2\right)\sin(k_c^1 x)}{\cos^2(k_c^1 l^1)\left[\kappa_3^1 - 2\kappa_1^2 + \hat{Z}^2\left(\kappa_1^2\kappa_3^1 - 2(\kappa_1^2)^2 + 2(\kappa_2^2)^2\right)\right]} + \frac{M_L^1(r)}{M^1}\left[\frac{\hat{Q}^1_{\text{in}}\sin(k_c^1 l^1)}{\cos(k_c^1 l^1)}\sin(k_c^1 x) + \hat{Q}^1_{\text{in}}\cos(k_c^1 x)\right], \tag{44}$$

$$\hat{p}_2(x) = -\frac{\hat{Q}^1_{\text{in}}\left(1+\hat{Z}^2\kappa_1^2\right)\left[\sin(k_c^2 l^2)\cos(k_c^2 x) - \cos(k_c^2 l^2)\sin(k_c^2 x)\right] + \hat{Q}^1_{\text{in}}\hat{Z}^2\kappa_2^2\sin(k_c^2 x)}{\sin(k_c^2 l^2)\cos(k_c^1 l^1)\left[\kappa_3^1 - 2\kappa_1^2 + \hat{Z}^2\left(\kappa_1^2\kappa_3^1 - 2(\kappa_1^2)^2 + 2(\kappa_2^2)^2\right)\right]}, \tag{45}$$

$$\hat{Q}_2(x) = -M^2\frac{\hat{Q}^1_{\text{in}}\left(1+\hat{Z}^2\kappa_1^2\right)\left[\sin(k_c^2 l^2)\sin(k_c^2 x) + \cos(k_c^2 l^2)\cos(k_c^2 x)\right] - \hat{Q}^1_{\text{in}}\hat{Z}^2\kappa_2^2\cos(k_c^2 x)}{\sin(k_c^2 l^2)\cos(k_c^1 l^1)\left[\kappa_3^1 - 2\kappa_1^2 + \hat{Z}^2\left(\kappa_1^2\kappa_3^1 - 2(\kappa_1^2)^2 + 2(\kappa_2^2)^2\right)\right]}, \tag{46}$$

$$\hat{u}_2(r,x) = M_L^2(r)\left(\frac{-\hat{Q}^1_{\text{in}}\left(1+\hat{Z}^2\kappa_1^2\right)\left[\sin(k_c^2 l^2)\sin(k_c^2 x) + \cos(k_c^2 l^2)\cos(k_c^2 x)\right] + \hat{Q}^1_{\text{in}}\hat{Z}^2\kappa_2^2\cos(k_c^2 x)}{\sin(k_c^2 l^2)\cos(k_c^1 l^1)\left[\kappa_3^1 - 2\kappa_1^2 + \hat{Z}^2\left(\kappa_1^2\kappa_3^1 - 2(\kappa_1^2)^2 + 2(\kappa_2^2)^2\right)\right]}\right). \tag{47}$$

Full aorta model

We consider a 20-artery model representing the aorta and its first generation of main branches (Fig. 5). An analytical solution for this model is calculated in Appendix II.

3 Results

We compare the solutions given by our new GDEM analytical approach, for blood modeled as a Newtonian fluid, with those obtained using the linear 1-D[2] and nonlinear 3-D[17] numerical formulations in a series of idealized models of the human common carotid artery, upper thoracic aorta, aortic bifurcation, and full aorta.

In both, 1-D and 3-D models used for comparison, the arterial wall was considered to be a thin, incompressible, homogeneous, isotropic and linear elastic membrane. In the 1-D model the arterial wall deformation was assumed to be axisymmetric, whereas, in the 3-D formulation no assumptions regarding axisymmetry were made. The 3-D model reproduces Womersley-like profiles, whereas 1-D model imposes a shape of the velocity profile.

3.1 Common carotid artery

The common carotid artery is simulated as a single vessel with uniform properties coupled to a three-element lumped parameter model of the rest of the systemic circulation, as described in Xiao *et al.*[55] The parameters of this model are given in Table 1. The inflow boundary condition, $Q_{\text{in}}(t)$, was measured *in vivo* and is shown in Fig. 6.

Figure 6 also shows the predictions of pressure, flow rate, and velocity profiles at several sites given by the new GDEM (Eqs. (36), (37), and (38)), and existing 1-D and 3-D formulations with compatible geometrical and mechanical properties and identical inflow and outflow boundary conditions.[55] From the pressure at a given site, we also compute the change in radius, Δr, from diastole, given by Hooke's law for a tube (Eq. (63) in Appendix I). Results show an excellent agreement between the three models: average relative errors for the new GDEM are smaller than 1% for pressure, flow and change in radius, while the average relative error for the pressure difference between the inlet and the outlet is less than 5%, with respect to both the numerical 1-D and 3-D solutions. Relative errors were calculated as described in Appendix III.

Velocity profiles predicted by GDEM are very close to both 1-D and 3-D profiles. One might wonder why there are some discrepancies in the profiles while there is an almost perfect agreement for the flow as a function of time. The source of these discrepancies is that our model defines flow as a constant cross sectional area times the time-dependent average velocity, while the other two models define

the flow as a time-depending cross-sectional area times a time-depending average velocity. Agreement is clearly better between the GDEM profiles and the 3-D profiles since the shape of the velocity profile is imposed – rather than calculated – in the 1-D model.

3.2 Upper thoracic aorta

The thoracic aorta from the aortic root to the descending aorta is simulated as a single vessel with uniform properties coupled to a three-element lumped parameter model of the rest of the systemic circulation.[55] The parameters of this model are displayed in Table 2 and the *in vivo* inflow boundary condition, $Q_{\text{in}}(t)$, is shown in Fig. 7.

As for the common carotid artery, Fig. 7 also shows the predictions of pressure, flow rate, change in radius, and velocity profiles at several points obtained using the new GDEM (Eqs. (36), (37), and (38)), and existing 1-D and 3-D formulations with compatible geometrical and mechanical properties and identical inflow and outflow boundary conditions.[55] The GDEM is able to predict similar waveforms. The smallest relative errors are for the pressure and the largest for the pressure difference. Average relative errors are all smaller than 1.5% for pressure, flow and change in radius, and smaller than 5% for the pressure difference between the inlet and the outlet of the vessel. Velocity profiles predicted by GDEM are closer to 3-D than 1-D profiles.

3.3 Aortic bifurcation

We consider a single-bifurcation model of the abdominal aorta branching into the two iliac arteries.[55] Both iliac arteries are coupled to three-element lumped parameter models of the rest of the systemic circulation. The parameters of this model are shown in Table 3; the *in vivo* inflow boundary condition, $Q_{\text{in}}(t)$, is shown in Fig. 8.

Figure 8 compares the predictions of pressure, flow rate, change in radius and velocity profiles at several sites computed using the GDEM (Eqs. (42), (43), (44), (45), (46), and (47)), and existing 1-D and 3-D formulations with compatible geometrical and mechanical properties and identical inflow and outflow boundary conditions.[55] As for the study of the common carotid artery and the upper thoracic aorta, there is an excellent agreement among the three models: average relative errors for the new GDEM solutions are smaller than 2% for pressures and flows, and smaller than 8.6% for change in radius, relative to both the 1-D and 3-D results. Velocity profiles predicted by GDEM are closer to 3-D than 1-D profiles.

3.4 Full aorta model

The last idealized model considered to test the analytical GDEM formulation is a bifurcating tree of the aorta and its larger branches represented by 20 arterial segments.[55] The network topology of this full-aorta model is shown in Fig. 5. General parameters of this model are given in Table 4; model parameters for each arterial segment are given in Table 5. At the inlet of the ascending aorta, the flow rate measured *in vivo*, $Q_{\text{in}}(t)$, is prescribed as the inflow boundary condition. Terminal vessels are coupled to three-element lumped parameter models simulating blood flow and pressure in downstream vessels. Appendix II shows how the analytical response function matrix, $\mathbf{K}$, is obtained following the methodology described in Section 2.2. Symbolic inversion of the matrix was done using Mathematica 7. Appendix II includes an analytical expression for the pressure at the first node. Figure 9 shows comparisons of pressure and flow waveforms at multiple locations obtained using the new GDEM model and numerical 1-D and 3-D approaches. Results shown excellent agreement between the three models: average relative errors for the new GDEM solutions are smaller than 2.1% for pressures and smaller than 2.3% for the flows, relative to both the 1-D and 3-D results.

4 Discussion

We have derived a new formulation of blood flow in the arterial network – called Generalized Darcy's Elastic Model (GDEM) – which can be fully solved analytically in frequency domain. The name comes from the field of porous media, in which there is a proportionality relation between flow and constant pressure gradient named Darcy's Law. In the field of pulsatile flows, in which a proportionality relation between flow and pressure gradient in frequency domain has been derived, the term Generalized Darcy's Law or Generalized Darcy's Model (GDM) is used. When elasticity is included, as we do here, the frequency-dependent pressure gradient varies along the flow direction. We have assumed that a GDM is valid locally and have therefore named the model GDEM.

We have assessed the accuracy of the GDEM by comparison against idealized models of the aorta and its largest branches. These models range from single-vessel models to network models simulating blood flow in the aorta and first generation of branches under normal physiological conditions. For all test cases, average relative errors smaller than 2.3% for the flow and 2.1% for pressure were observed between the new GDEM and existing computational 1-D and 3-D models. Our results show the ability of the GDEM to reproduce the main features of pulse waveforms in networks of large arteries under normal physiological conditions.

4.1 Model features

We have combined a 0-D generalized Darcy's model (GDM) for rigid tubes that takes into account the linear dynamics of a momentum equation for the axial velocity, for Newtonian or Maxwellian fully developed fluids, with a 1-D model derived from the 2-D continuity equation and a Hooke' law that relates the pressure and the displacements of the tube in the radial direction. For this, we have assumed that the most important contribution for variations of the axial velocity along the flow direction, within a vessel, comes from the pressure. We have therefore created

the GDEM by assuming that Darcy's model for rigid tubes is locally valid for any pressure gradient. The continuity equation and Hooke's law combined with the GDM allow one to write an harmonic equation for the pressure in frequency domain. Once this equation is solved with known boundary conditions at the vessel extremes, the pressure gradient can be calculated at any point along a vessel axis. Then the existing GDM enables calculation of the flow and the velocity profiles.

We have assumed that the GDEM governing equations for a single vessel, are valid for each vessel within a network. We have imposed flow conservation and pressure continuity at the nodes. Consistent with our linear approach, the dynamic part of pressure ($1/2\rho U^2$) has been neglected.

We have written general equations for a network with multiple input and output boundary conditions, with flow waveforms prescribed at the inputs and outputs coupled to 3-element Windkessel models. To validate the GDEM, we have considered a single input for all test cases with the prescribed inflow waveform measured *in vivo* at either the aortic root or common carotid artery.

Our model does not impose a velocity profile, the GDEM for Newtonian fluids gives the Womerseley profile. However, the GDEM allows for a pressure gradient variation along the flow direction, that when substituted into the velocity equation gives different profiles for different positions within a vessel. The GDEM has been presented for a Maxwell fluid in order to have the possibility of studying blood viscoelastic effects, which might be relevant in small arteries. In order to validate GDEM with existing results, we have used the particular case of a Newtonian fluid in the present paper.

4.2 Model limitations

Our model has two main limitations: it considers linear terms in order to work in frequency domain and it considers axisymmetry of the flow since it uses a 1-D approach. The range of applicability of the proposed methodology has been validated for the aorta and its main branches and the agreement with 3-D results

with realistic geometry (curvature, torsion and tapering) indicates that, at least under normal physiological conditions -in the absence of stenosis or aneurisms-, our 1-D approach and the linearization are reasonable approximations in the validated range. We suspect that around valves, large obstructions, and large stenosis the 1-D linear formulation will be less accurate. However, this still needs to be tested.

We have provided an analytical solution for cylindrical segments without any tapering. This is not a serious limitation since tapering can be simulated in a discrete fashion by dividing a segment into several sub-segments, each with slightly different radius. For instance, we have followed this approach for the full-aorta model, for which the aorta was divided into several segments, each with distint radius and elastic properties.

We have neglected vessel wall viscoelasticity, which could be included into our model by considering a frequency-dependent Young modulus $E(\omega)$. Our frequency-domain formulation could be modified to include this type of dependence, if C in Eq. (6) contained $E(\omega)$ instead of a constant E.

4.3 Analyticity advantages

Once the pressures at each node of the network are known, our new GDEM can be used to obtain analytically pressure and flow waveforms, as well as velocity profiles at any point. An analytical solution allows for a visual inspection of where the different physical parameters enter the different terms, for example in Eqs. (36), (37) and (38) for a single vessel one could see how the elastic parameter C enters the equations, by watching at how it enters k_c and M in such equations. It also enables to identify the contribution of each vessel to the elements of the matrix $\mathbf{K}$. See for example the matrix for the full-aorta model in Appendix II. If one wanted to analyse where the properties of the celiac artery (Vessel 14), to put an example, entered the response, one could easily identify the two diagonal terms and the two off-diagonal terms that contain properties of this particular vessel.

Analyticity also allows for fast computations. For a given network, analytical inversion of $\mathbf{K}$ has to be done only once. Then, for different values of the properties of blood and the blood vessels, the solution can be evaluated numerically without having to solve the system of equations each time as in numerical approaches. Symbolic inversion to obtain $\mathbf{K^{-1}}$ is easily done for small networks, for instance, for our 20-vessel full aorta model, symbolic inversion of the 20x20 matrix in Mathematica 7, using LU decomposition, run in an Intel CORE i5-3427U processor @1.8GHz in Ubuntu 14.04 LTS with 4GB of RAM at 1600MHz took 0.93 seconds of machine time. Moreover, our analytical approach also enables quick computation of the solution for different inflows, again, without having to recalculate $\mathbf{K}^{-1}$ for each incident boundary condition. These advantages of our analytical approach are relevant in studies for which hundreds to thousands of simulations are required; *e.g.* to create virtual populations of pulse waveforms,[54] and in uncertainty and sensitivity analysis of pulse waves.[16,28]

4.4 Results for single artery models

We started by testing our new GDEM in two single-vessel benchmark test cases representing the common carotid artery (Fig. 6) and upper thoracic aorta (Fig. 7), under normal physiological conditions. These are idealized test cases that do not account for vessel curvature, torsion, tapering or branching, which are all properties found in anatomically-correct aortas and carotid arteries. Under these assumptions, the analytical GDEM was able to capture the main features of pressure and flow waveforms provided by the numerical 1-D and 3-D models, as well as the velocity profiles computed by the 3-D model with an axisymmetric velocity profile prescribed at the inlet.[55] Relative errors were consistently smaller for the carotid than the aorta model. This is due to inertial forces playing a larger role in the aorta model; the peak Reynolds number is nearly an order of magnitude greater in the aorta.[55]

4.5 Results for network models

The two additional test cases that we have used to assess the analytical GDEM contain arterial bifurcations – a key anatomical feature for blood flow modelling in the arterial tree. These are a single-bifurcation model and the full-aorta model with multiple bifurcations. The full-aorta GDEM model also contains vessel tapering in an approximated way by modelling it as segments of different radii. In both test cases, the GDEM is able to reproduce the main features of pressure and flow waveforms with errors smaller than 2.1% for pressure and 2.3% for the flow, relative to the corresponding results obtained using the 1-D and 3-D numerical approaches (Figs. 8 and 9). Both approaches simulate vessel tapering, and the 3-D approach, simulates the curvature and torsion of the aortic arch. Discrepancies between the analytical GDEM and numerical 1-D results arise from the different assumptions of the models, for instance the 1-D formulation assumes a velocity profile whereas the GDEM gives locally a Womersley profile. Discrepancies between GDEM and numerical 3-D results arise from the assumptions and simplifications of the GDEM. We note, however, that such differences between the analytical and existing numerical solutions may be irrelevant for clinical applications, as the observed discrepancies between models will be negligible with respect to uncertainties from various physical and physiological sources. See for example Chen *et al.* [10] for an uncertainty quantification of simulated pressure waveforms.

Further tests of our new GDEM are required to asses its accuracy to simulate pulse waveforms and velocity profiles in anatomically-correct arterial geometries, including comparisons against in-vivo hemodynamic data. It should be tested with a more realistic model than the purely elastic linear-arterial wall considered in Xiao et al.[55] In addition, the GDEM should be tested against a non-linear 1-D formulation that does not impose a shape for the velocity profiles (see e.g. Bessems *et al.* [6]). Lastly, accuracy of the GDEM should be assessed against 3-D data computed using an Arbitrary Lagrangian Eulerian (ALE) formulation.

4.6 Conclusions and Perspectives

We have shown that arterial pulse wave haemodynamics in large arteries can be accurately simulated using a generalized Darcy's elastic model for which a full analytical solution in frequency domain exists. Our new model has been assessed in a series of benchmark test cases with an increasing degree of complexity, for which numerical 1-D and 3-D pulse waveforms are available. Results have shown the ability of our analytical GDEM solution to capture the main features of pulse wave propagation in single arterial vessels as well as in networks of vessels with tapering, curvature and torsion. This study provides additional support for the use of 1-D reduced-order modeling to accurately simulate arterial pulse wave haemodynamics at a very low computational cost.

Our results suggest that the GDEM has reasonable accuracy to explore the role of different physical parameters of the cardiovascular system in shaping blood pressure and flow waveforms. The analyticity of our model has also the advantage of decreasing the computational cost of arterial pulse wave simulations, which is important in studies for which hundreds to thousands of simulations are required.[16,28,54]

Acknowledgements The authors would like to thank Drs Nan Xiao and Alberto Figueroa for providing all 3-D data used in this study. JFG acknowledges financial support from CONACYT (Mexico) through fellowship 240094. JA gratefully acknowledges the support of an EPSRC project grant (EP/K031546/1), the Centre of Excellence in Medical Engineering (funded by the Wellcome Trust and EPSRC under grant number WT 088641/Z/09/Z), and the National Institute for Health Research (NIHR) Biomedical Research Centre at Guys and St Thomas' NHS Foundation Trust in partnership with King's College London. ECP declares that the research leading to these results has received funding from the European Union Seventh Framework Programme (FP7-PEOPLE-2011-IIF) under grant agreement N0 301214, as well as financial support from CONACYT (Mexico) through projects 83149 and 219584.

References

[1] Alastruey, J., A. Khir, K. Matthys, P. Segers, S. Sherwin, P. Verdonck, K. Parker, and J. Peiró. Pulse wave propagation in a model human arterial network: Assessment of 1-D visco-elastic simulations against *in vitro* measurements. *J. Biomech.* 44: 2250–2258, 2011.

[2] Alastruey, J., K. Parker, and S. Sherwin. "Arterial pulse wave haemodynamics." In: *11th International Conference on Pressure Surges*, edited by S. Anderson. Lisbon: Virtual PiE Led t/a BHR Group, 2010, pp. 401-442.

[3] Alastruey, J., S. Moore, K. Parker, T. David, J. Peiró, and S. Sherwin. Reduced modelling of blood flow in the cerebral circulation: Coupling 1-D, 0-D and cerebral auto-regulation models. *Int. J. Numer. Meth. Fluids* 56:1061–1067, 2008.

[4] Avolio, A. Multi-branched model of the human arterial system. *Med. and Biol. Engng. and Comput.* 18:709-718, 1980.

[5] Azer, K., and C. Peskin. A one-dimensional model of blood flow in arteries with friction and convection based on the Womersley velocity profile. *Cardiov. Eng.* 7:5173, 2007.

[6] Bessems, D., C. Giannopapa, M. Rutten, and F. van de Vosse. Experimental validation of a time-domain-based wave propagation model of blood flow in viscoelastic vessels. *J. Biomech.* 41, 284–291, 2008.

[7] Blanco, P., S. Watanabe, E. Dari, M. Passos, and R. Feijóo. Blood flow distribution in an anatomically detailed arterial network model: criteria and algorithms. *Biomech. Model. Mechanobiol.* 13:1303–1330, 2014.

[8] Čanić, S., and E. Kim. Mathematical analysis of the quasilinear effects in a hyperbolic model of blood flow through compliant axi-symmetric vessels. *Math. Meth. Appl. Sci.* 26:1161–1186, 2003.

[9] Cebral, J., M. Castro, J. Burgess, R. Pergolizzi, M. Sheridan, and C. Putman. Characterization of cerebral aneurysms for assessing risk of rupture by using patient-specific computational hemodynamics models. *Am. J. Neuroradiol.* 26(10):2550–2559, 2005.

[10] Chen, P., A. Quarteroni, and G. Rozza. Simulation-based uncertainty quantification of human arterial network hemodynamics. *Int. J. Numer. Meth. Biomed. Engng.* 29:698–721, 2013.

[11] Coccarelli, A., and P. Nithiarasu. A robust finite element modeling approach to conjugate heat transfer in flexible elastic tubes and tube networks. *Numer. Heat Tr. A-Appl.* 67:513–530, 2015.

[12] Collepardo Guevara, R., and E. Corvera Poiré. Controlling viscoelastic flow by tuning frequency during occlusions. *Phys. Rev. E* 76, 026301, 2007.

[13] Danielsen, M., and J. Ottesen. "A cardiovascular model. " In: *Applied Mathematical Models in Human Physiology*, edited by J. Ottesen, M. Olufsen, and J. Larsen. Philadelphia: SIAM monographs on mathematical human physiology, 2004, pp. 137-155.

[14] del Río, J. A., M. López de Haro, and S. Whitaker. Enhancement in the dynamic response of a viscoelastic fluid flowing in a tube. *Phys. Rev. E* 58, 6323-6327, 1998.

[15] del Río, J. A., M. López de Haro, and S. Whitaker. Erratum: Enhancement in the dynamic response of a viscoelastic fluid flowing in a tube [Phys. Rev. E 58, 6323 (1998)]. *Phys. Rev. E* 64, 039901, 2001.

[16] Eck, V., J. Feinberg, H. Langtangen, and L. Hellevik. Stochastic sensitivity analysis for timing and amplitude of pressure waves in the arterial system. *Int. J. Numer. Meth. Biomed. Eng.* 31 (EPub), 2015.

[17] Figueroa, C., I. Vignon-Clemental, K. Jansen, T. Hughes, and C. Taylor. A coupled momentum method for modeling blood flow in three-dimensional deformable arteries. *Comp. Meth. App. Mech. Eng.* 195:5685–5706, 2006.

[18] Flores Gerónimo, J., A. Meza Romero, R. D. M. Travasso, and E. Corvera Poiré. Flow and anastomosis in vascular networks. *J. Theor. Biol.* 317:257, 2013.

[19] Flores Gerónimo, J., E. Corvera Poiré, J. A. del Río, and M. López de Haro. A plausible explanation for heart rates in mammals. *J. Theor. Biol.* 265, 599-603, 2010.

[20] Formaggia, L., D. Lamponi, and A. Quarteroni. One-dimensional models for blood flow in arteries. *J. Eng. Math.* 47:251–276, 2003.

[21] Frank, O. Die Grundform des arteriellen Pulses. *Erste Abhandlung Mathematische Analyse Z. Biol.* 37:483–526, 1899.

[22] Fung, Y. C. *Biomechanics, Circulation*. New York: Springer-Verlag, 1984.

[23] Gallo D., D. A. Steinman, and U. Morbiducci. An Insight into the mechanistic role of the common carotid artery on the hemodynamics at the carotid bifurcation. *Ann Biomed Eng* 43, 68-61, 2015.

[24] Gerbeau, J. F., M. Vidrascu, and P. Frey. Fluid-structure interaction in blood flows on geometries based on medical imaging. *Comp. Struct.* 83(2-3):155–165, 2005.

[25] Hale, J. F., D. A. McDonald and J. R. Womersley. Velocity profiles of oscillating arterial flow, with some calculations of viscous drag and the Reynolds number. *J. Physiol.* 128:629-64,1955.

[26] Hellevik, L. R., J. Vierendeels, T. Kiserud, N. Stergiopulos, F. Irgens, and E. Dick. An assessment of ductus venosus tapering and wave transmission from the fetal heart. *Biomech. Model. Mechanobiol.* 8(6):509–517,2009.

[27] Huberts, W., K. V. Canneyt, P. Segers, S. Eloot, J. Tordoir, P. Verdonck, F. van de Vosse, and E. Bosboom. Experimental validation of a pulse wave propagation model for predicting hemodynamics after vascular access surgery. *Med. Eng. & Phys.* 45:1684–1691, 2012.

[28] Huberts, W., C. de Jonge, W.P.M. van der Linden, M.A. Inda, J.H.M. Tordoir, F.N. van de Vosse, and E. Bosboom. A sensitivity analysis of a personalized pulse wave propagation

model for arteriovenous fistula surgery. Part A: Identification of most influential model parameters. *J. Biomech.* 35:810–826, 2013.

[29] Hughes, T., and J. Lubliner. On the one-dimensional theory of blood flow in the larger vessels. *Math. Biosciences* 18:161–170, 1973.

[30] Liang, F., S. Takagi, R. Himeno, and H. Liu. Biomechanical characterization of ventricular–arterial coupling during aging: A multi-scale model study. *J. Biomech.* 42:692–704, 2009.

[31] Mazumbdar, J. *An introduction to Mathematical Physiology and Biology.* New York: Second Edition, Cambridge University Press, 1999.

[32] Müller, L., and E. Toro. Well balanced high order solver for blood flow in networks of vessels with variable properties. *Int. J. Numer. Meth. Biomed. Engng.* 29:1388–1411, 2013.

[33] Mynard, J., and P. Nithiarasu. A 1D arterial blood flow model incorporating ventricular pressure, aortic valve and regional coronary flow using the locally conservative Galerkin (LCG) method. *Commun. Numer. Meth. Eng.* 24:367–417, 2008.

[34] Nichols, W. W., and M. F. O'Rourke. *McDonalds Blood Flow in Arteries: Theoretical, Experimental, and Clinical Principles*, New York: Oxford University Press, Vol. 11, 2005.

[35] Olufsen, M., C. Peskin, W. Kim, E. Pedersen, A. Nadim, and J. Larsen. Numerical simulation and experimental validation of blood flow in arteries with structured-tree outflow conditions. *Ann. Biomed. Eng.* 28:1281-1299, 2000.

[36] Papadakis, G. Wave propagation in tapered vessels: new analytic solutions that account for vessel distensibility and fluid compressibility. *J. Pressure Vessel Technol.* 136:014501 1-9, 2014.

[37] Perktold, K., and G. Rappitsch. Computer simulation of local blood flow and vessel mechanics in a compliant carotid artery bifurcation model. *Journal of Biomechanics* 28(7):845–56, 1995.

[38] Quarteroni, A., M. Tuveri, A. Veneziani. Computational vascular fluid dynamics: Problems, models and methods. *Comput. Visual. Sci.* 2:163–197, 2000.

[39] Reymond, P., F. Merenda, F. Perren, D. Rüfenacht, and N. Stergiopulos. Validation of a one-dimensional model of the systemic arterial tree. *Am. J. Physiol. Heart Circ. Physiol.* 297:H208–H222, 2009.

[40] Reymond, P., Y. Bohraus, F. Perren, F. Lazeyras, and N. Stergiopulos. Validation of a patient-specific one-dimensional model of the systemic arterial tree. *Am. J. Physiol. Heart Circ. Physiol.* 301:H1173–H1182, 2011.

[41] Saito, M., Y. Ikenaga, M. Matsukawa, Y. Watanabe, T. Asada, and P. Y. Lagrée. One-dimensional model for propagation of a pressure wave in a model of the human arterial network: Comparison of theoretical and experimental results. *J. Biomech. Eng.* 133:121 005, 2011.

[42] Sherwin, S., L. Formaggia, J. Peiró, and V. Franke. Computational modelling of 1D blood flow with variable mechanical properties and its application to the simulation of wave propagation in the human arterial system. *Int. J. Numer. Meth. Fluids* 43:673–700, 2003.

[43] Smith, N., A. Pullan, and P. Hunter. An anatomically based model of transient coronary blood flow in the heart. *SIAM J. Appl. Math.* 62:990–1018, 2002.

[44] Steele, B., J. Wan, J. Ku, T. Hughes, and C. Taylor. In vivo validation of a one-dimensional finite-element method for predicting blood flow in cardiovascular bypass grafts. *IEEE Trans. Biomed. Eng.* 50:649–656, 2003.

[45] Steinman, D., J. Milner, C. Norley, S. Lownie, and D. Holdsworth. Image-based computational simulation of flow dynamics in a giant intracranial aneurysm. *Am. J. Neuroradiol.* 24(4):559–566, 2003.

[46] Stergiopulos, N., B. Westerhof, and N. Westerhof. Total arterial inertance as the fourth element of the windkessel model. *Am. J. Physiol.* 276:H81–H88, 1999.

[47] Stergiopulos, N., D. Young, and T. Rogge. Computer simulation of arterial flow with applications to arterial and aortic stenoses. *J. Biomech.* 25:1477–1488, 1992.

[48] Taylor, C. A., T. J. R. Hughes, and C. K. Zarins. Finite element modeling of blood flow in arteries. *Comput. Methods Appl. Mech. and Engrg.* 7825:(97), 1998.

[49] Torres Rojas, A. M., A. Meza Romero, I. Pagonabarraga, R. D. M. Travasso, and E. Corvera Poiré. Obstructions in vascular networks: Relation between network morphology and blood supply. *PLOS One* 10:e0128111, 2015.

[50] Ursino, M. Interaction between carotid baroregulation and the pulsating heart: a mathematical model. *Am. J. Heart Circ. Physiol.* 275:H1733–H1747, 1998.

[51] Vignon-Clementel, I., C. Figueroa, K. Jansen, and C. Taylor. Outflow boundary conditions for three-dimensional finite element modeling of blood flow and pressure in arteries. *Comp. Meth. App. Mech. Eng.* 195:3776–3796, 2006.

[52] Westerhof, N., J. W. Lankhaar, and B. Westerhof. The arterial Windkessel. *Med. & Biol. Eng. & Comput.* 47:131–141, 2009.

[53] Willemet, M., V. Lacroix, and E. Marchandise. Validation of a 1D patient-specific model of the arterial hemodynamics in bypassed lower-limbs: Simulations against in vivo measurements. *Med. Eng. Phys.* 35:1573–1583, 2013.

[54] Willemet, M., and J. Alastruey. A database of virtual healthy subjects to assess the accuracy of foot-to-foot pulse wave velocities for estimation of aortic stiffness. *Am. J. Physiol. Heart Circ. Physiol.* 309:H663–H675, 2015.

[55] Xiao, N., J. Alastruey, and C. Figueroa. A systematic comparison between 1-D and 3-D hemodynamics in compliant arterial models. *Int. J. Numer. Meth. Biomed. Eng.* 30, 204–231, 2014.

Tables

Table 1: Model parameters of the common carotid artery.

Property	Value
Length, L	126 mm
Radius at diastolic pressure, R_{d}	3 mm
Average radius, R_0	3 mm
Wall thickness, h	0.3 mm
Blood density, ρ	$1,060$ Kg m^{-3}
Blood viscosity, η	4 mPa s
Young's modulus, E	700.0 kPa
Diastolic pressure, P_{d}	10.933 kPa
Outflow pressure, P_{out}	0
Windkessel resistance, R_1	$2.4875 \cdot 10^8$ Pa s m^{-3}
Windkessel compliance, C	$1.7529 \cdot 10^{-10}$ m^3 Pa^{-1}
Windkessel resistance, R_2	$1.8697 \cdot 10^9$ Pa s m^{-3}

Parameters were taken from Xiao *et al.*[55] The average radius, R_0, was computed by time and space averaging of the 1-D results by Xiao *et al.*[55]

Table 2: Model parameters of the upper thoracic aorta.

Property	Value
Length, L	24.137 cm
Radius at diastolic pressure, R_{d}	1.2 cm
Average radius, R_0	1.27 cm
Wall thickness, h	1.2 mm
Blood density, ρ	$1,060$ Kg m^{-3}
Blood viscosity, η	4 mPa s
Young's modulus, E	400.0 kPa
Diastolic pressure, P_{d}	9.46 kPa
Outflow pressure, P_{out}	0
Windkessel resistance, R_1	$1.1752 \cdot 10^7$ Pa s m^{-3}
Windkessel compliance, C	$1.0163 \cdot 10^{-8}$ m^3 Pa^{-1}
Windkessel resistance, R_2	$1.1167 \cdot 10^8$ Pa s m^{-3}

Parameters were taken from Xiao *et al.*[55] The average radius, R_0, was computed by time and space averaging of the 1-D results by Xiao *et al.*[55]

Table 3: Model parameters of the aortic bifurcation.

Property	Aorta	Iliac
Length, L	8.6 cm	8.5 cm
Radius at diastolic pressure, R_{d}	0.86 cm	0.60 cm
Average radius, R_0	0.89 cm	0.615 cm
Wall thickness, h	1.032 mm	0.72 mm
Blood density, ρ	$1,060$ Kg m^{-3}	
Blood viscosity, η	4 mPa s	
Young's modulus, E	500.0 kPa	700.0 kPa
Diastolic pressure, P_{d}	9.1 kPa	9.1 kPa
Outflow pressure, P_{out}	–	0
Windkessel resistance, R_1	–	$6.8123 \cdot 10^{7}$ Pa s m^{-3}
Windkessel compliance, C	–	$3.6664 \cdot 10^{-10}$ m^{3} Pa^{-1}
Windkessel resistance, R_2	–	$3.1013 \cdot 10^{9}$ Pa s m^{-3}

Parameters were taken from Xiao *et al.*[55] The average radius, R_0, was computed by time and space averaging of the 1-D results by Xiao *et al.*[55]

Table 4: General parameters of the full-aorta model.

Property	Value
Blood density, ρ	$1,060$ Kg m^{-3}
Blood viscosity, η	4.0 mPa s
Diastolic pressure, P_{d}	9.5 kPa
Outflow pressure, P_{out}	0

Parameters were taken from Xiao *et al.*[55]

Table 5: Parameters of the full-aorta model.

Arterial segment	Length (cm)	$R_{\rm d}$ (mm)	R_0 (mm)	E (kPa)	R_1 (10^7 Pa s m^{-3})	R_2 (10^8 Pa s m^{-3})	C (10^{-10} m^3 Pa^{-1})
1. Ao I	7.0357	14.55	14.59	372.2	-	-	-
2. Ao II	0.8	13.8	13.8	384.2	-	-	-
3. Ao III	0.9	13.60	13.65	387.6	-	-	-
4. Ao IV	6.4737	12.9	12.9	400.0	-	-	-
5. Ao V	15.2	11.1	11.1	437.8	-	-	-
6. Ao VI	1.8	9.8	9.8	471.8	-	-	-
7. Ao VII	0.7	9.66	9.66	475.9	-	-	-
8. Ao VIII	0.7	9.585	9.6	478.1	-	-	-
9. Ao IX	4.3	9.31	9.31	486.5	-	-	-
10. Ao X	4.3	8.88	8.88	502.0	-	-	-
11. Brachiocephalic	3.4	6.35	6.35	612.0	5.1918	10.6080	8.6974
12. L com. carotid	3.4	3.6	3.6	860.4	19.1515	52.2129	1.7670
13. L subclavian	3.4	4.8	4.8	724.0	9.8820	13.0183	7.0871
14. Celiac	3.2	4.45	4.45	757.6	11.7617	7.5726	12.1836
15. Sup. mesenteric	6	3.75	3.75	839.6	17.4352	5.5097	16.7453
16. R renal	3.2	2.8	2.8	1000.4	34.1378	5.3949	17.1017
17. L renal	3.2	2.8	2.8	1000.4	34.1378	5.3949	17.1017
18. Inf. mesenteric	5	2.0	2.0	1224.2	74.0167	46.2252	1.9959
19. R com. iliac	8.5	6.0	6.0	633.3	5.9149	10.1737	9.0686
20. L com. iliac	8.5	6.0	6.0	633.3	5.9149	10.1737	9.0686

Parameters were taken from Xiao *et al.*,[55] where values for diastolic radii at the inlet ($R_d^{\rm in}$) and diastolic radii at the outlet ($R_d^{\rm out}$), are given. In our computations, we considered an averaged diastolic radius, $R_{\rm d} = (R_{\rm d}^{\rm in} + R_{\rm d}^{\rm out})/2$. Following Nichols and O'Rourke,[34] the wall thickness, h, was chosen to be 10% of $R_{\rm d}$. Following Xiao *et al.*,[55] the elastic moduli were calculated using $E = (3\rho c^2 R_{\rm d})/(2h)$, where the pulse wave velocity, c (in m/s), is given by the empirical relationship[39] $c = 13.3/(2R_{\rm d})^{0.3}$ with $R_{\rm d}$ measured in mm.

Figures

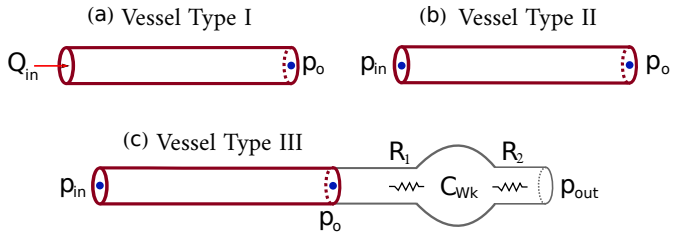

Fig. 1: Types of vessels according to their position within the network.

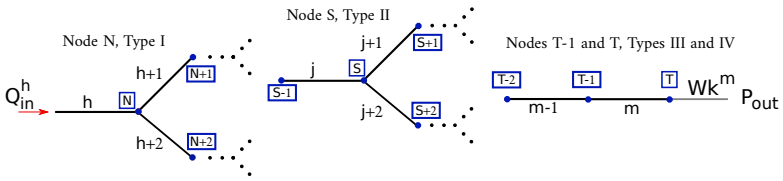

Fig. 2: Types of nodes according to the type of vessels that they connect.

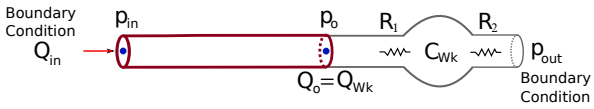

Fig. 3: Schematic representation of a single-vessel model, with an inflow and a three-element Windkessel as boundary conditions.

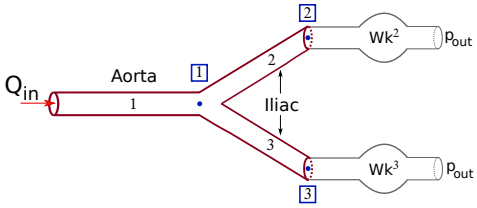

Fig. 4: Schematic representation of a single-bifurcation model.

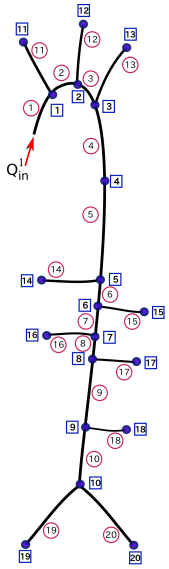

Fig. 5: Schematic representation of the 20-vessel full-aorta model.

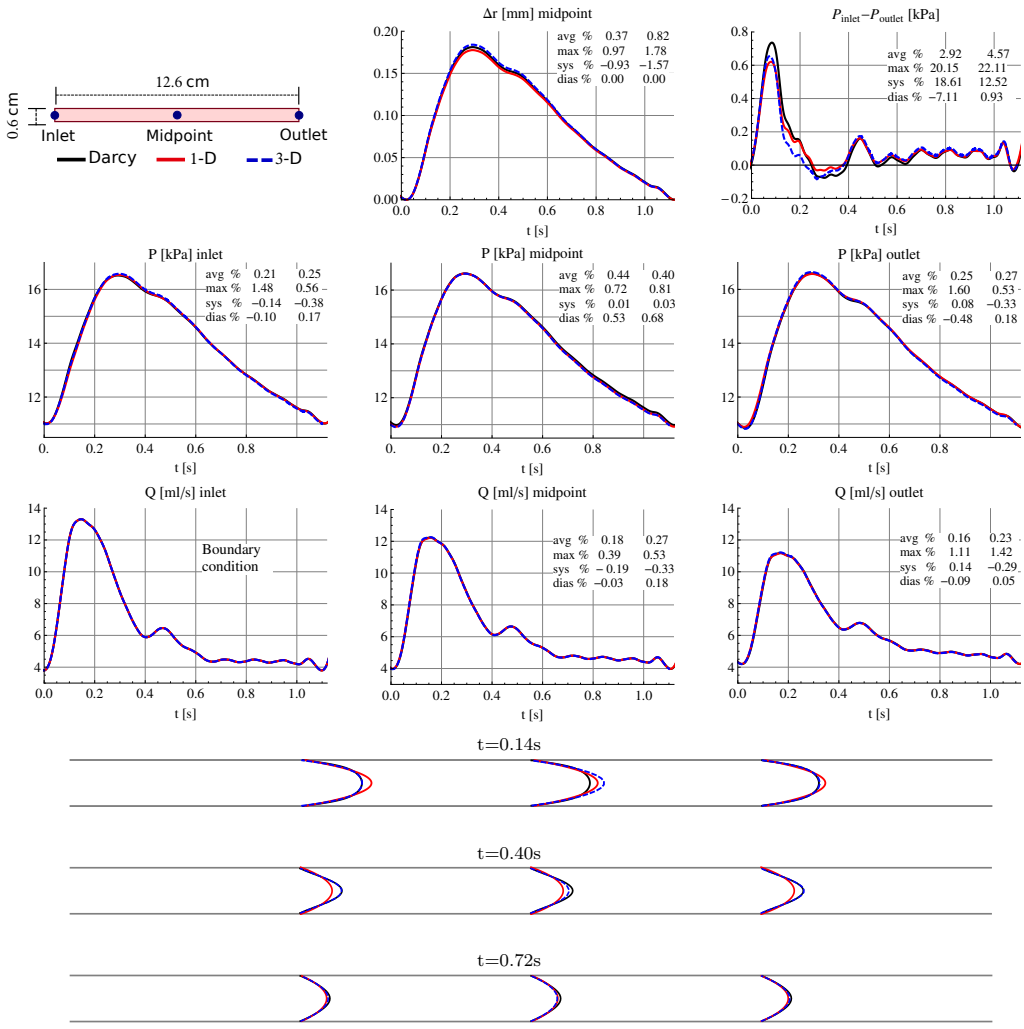

Fig. 6: Common carotid artery. Top: Pressure and flow rate with time at the inlet, midpoint and outlet, change in radius from the diastolic value with time at the midpoint, and pressure difference between inlet and outlet. Results are shown for the analytical GDEM solution (black solid lines) and the computational 1-D (red solid lines) and 3-D (dashed lines) solutions. Relative errors were calculated, as described in Appendix III, using first the 1-D model as a reference (first column in each figure) and then the 3-D model (second column in each figure). Bottom: Velocity profiles of the three models at three locations and three time points. The model parameters are shown in Table 1.

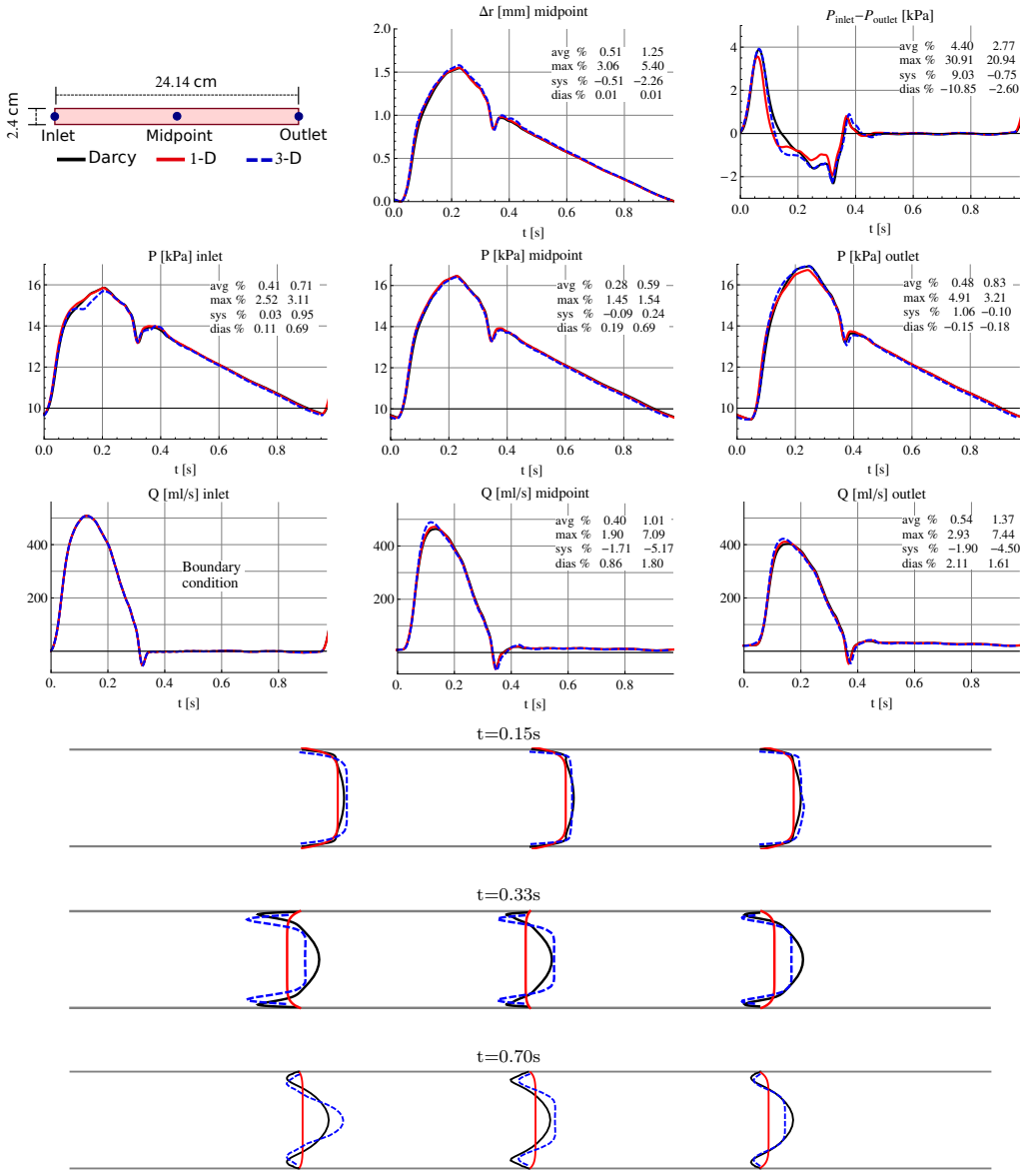

Fig. 7: Upper thoracic aorta. Top: Pressure and flow rate with time at the inlet, midpoint and outlet, change in radius from the diastolic value with time at the midpoint, and pressure difference between inlet and outlet. Results are shown for the analytical GDEM solution (black solid lines) and the computational 1-D (red solid lines) and 3-D (dashed lines) solutions. Relative errors were calculated using first the 1-D model as a reference (first column in each figure) and then the 3-D model (second column in each figure). Bottom: Velocity profiles of the three models at three locations and three time points. At times $t = 0.33$s and $t = 0.70$s, they have been scaled by factors of 3 and 4, respectively, in order to visualize them more easily. The model parameters are shown in Table 2.

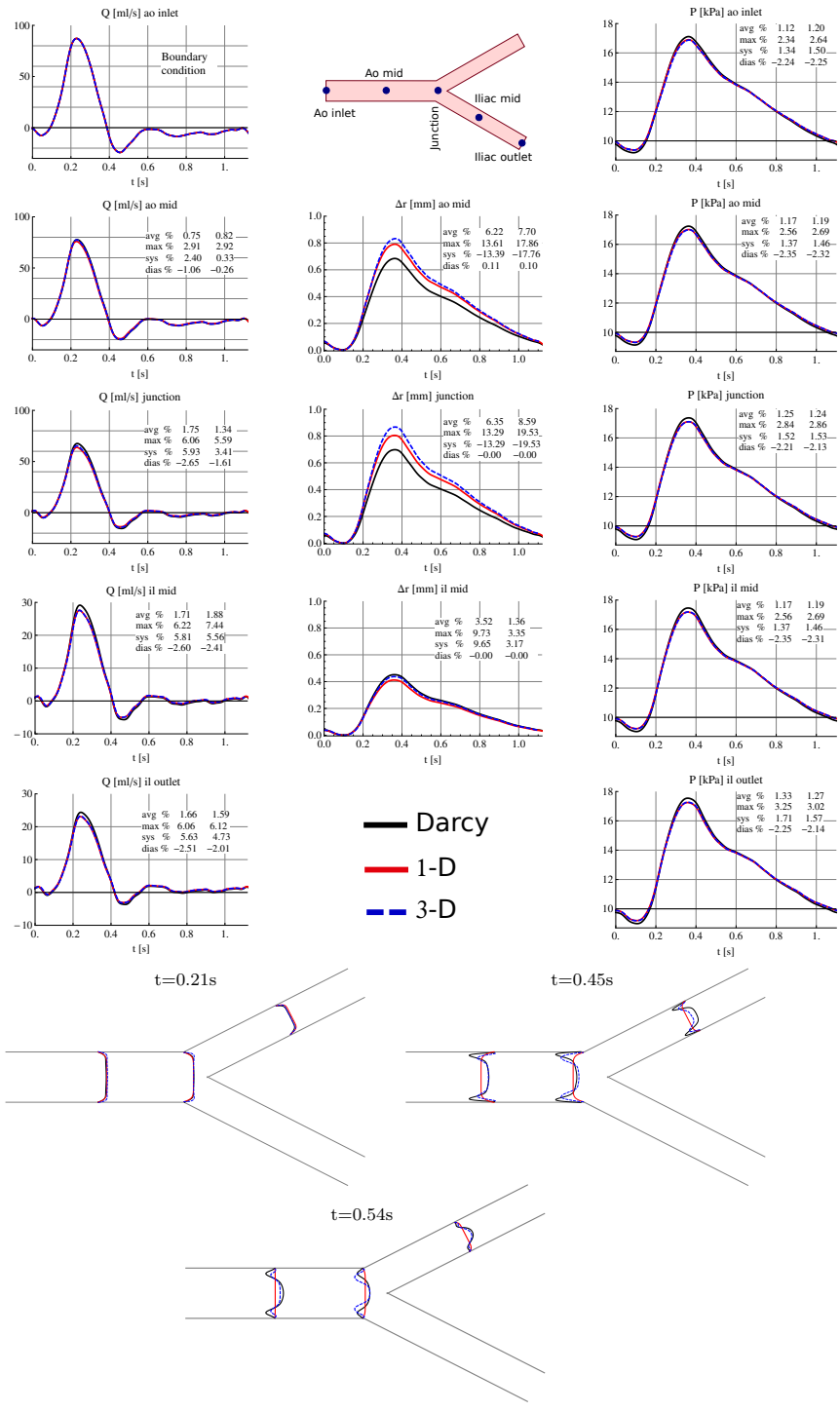

Fig. 8: Aortic bifurcation. Top: Pressure, flow rate and change in radius (from the diastolic value) with time at several locations. Results are shown for the analytical GDEM solution (black solid lines) and the computational 1-D (red solid lines) and 3-D (dashed lines) solutions. Relative errors were calculated, using first the 1-D model as a reference (first column in each figure) and then the 3-D model (second column in each figure). Bottom: Velocity profiles of the three models at three locations and three time points. At times $t = 0.45$s and $t = 0.54$s, they have been scaled by factors of 6 and 8, respectively, in order to visualize them more easily. The model parameters are shown in Table 3.

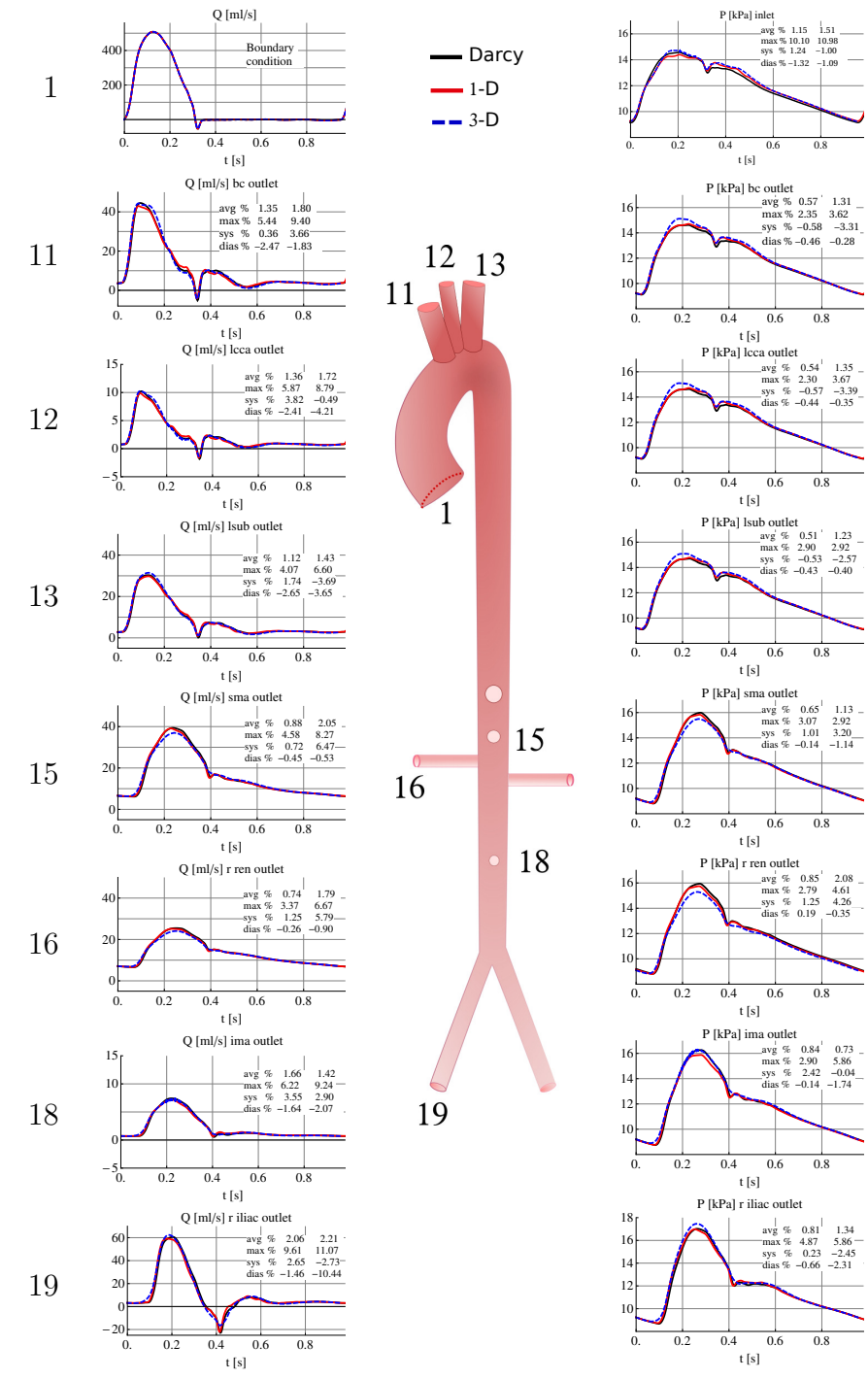

Fig. 9: Schematic representation of the full aorta. Pressure and flow rate with time at several locations. Results are shown for the analytical GDEM solution (black solid lines) and the computational 1-D (red solid lines) and 3-D (dashed lines) solutions. Relative errors were calculated using first the 1-D model as a reference (first column in each panel). and then the 3-D model (second column in each panel). The model parameters are shown in Tables 4 and 5.

Appendix I. Derivation of Generalized Darcy's Elastic Model (GDEM)

Equations (1), (2), (3) and (4) are obtained from the linearized momentum balance equations:

$$\rho \frac{\partial \mathbf{v}}{\partial t} = -\nabla p - \nabla \cdot \sigma, \tag{48}$$

where $\nabla \cdot \sigma$ represents the divergence of the viscous stress tensor. We consider a Maxwell fluid – the simplest fluid that presents viscoelastic behaviour – for which the fluid velocity and stress tensor are related by

$$t_r \frac{\partial \sigma}{\partial t} = -\eta \nabla \mathbf{v} - \sigma, \tag{49}$$

where t_r is the Maxwell relaxation time and is given by the ratio of the viscosity, η, and the elastic modulus, G; *i.e.* $t_r = \frac{\eta}{G}$. In the limit of zero relaxation time, Eq. (49) reduces to the constitutive equation for Newtonian fluids. We assume that the radial velocity is much smaller than the axial velocity, so that the momentum balance equations (48), together with the constitutive equations (49) are:

$$t_r \rho \frac{\partial^2 u}{\partial t^2} + \rho \frac{\partial u}{\partial t} = -\frac{\partial p}{\partial x} - t_r \frac{\partial^2 p}{\partial t \partial x} + \eta \left(\frac{\partial^2 u}{\partial r^2} + \frac{1}{r} \frac{\partial u}{\partial r} \right), \tag{50}$$

$$\frac{\partial p}{\partial r} = 0. \tag{51}$$

Equation (51) implies that pressure is only a function of x and t, and adjusts instantaneously to any point of a luminal cross-sectional area.

We then transform Eq. (50) to the frequency domain. For simplicity of notation we define $k = k(\omega)$, such that $k^2 = \frac{\rho}{\eta} \left(t_r \omega^2 + i\omega \right)$ and $B(x, \omega) = \left(\frac{1 - i\omega t_r}{\eta} \right) \frac{d\hat{p}}{dx}$. We obtain the following equation for the axial velocity $\hat{u}(x, r, \omega)$ in frequency domain,

$$r^2 \frac{\partial^2 \hat{u}}{\partial r^2} + r \frac{\partial \hat{u}}{\partial r} + k^2 r^2 \hat{u} = B r^2. \tag{52}$$

This is a Bessel equation of order zero, whose general solution is

$$\hat{u}(x,r,\omega) = aJ_0(kr) + bN_0(kr) + \hat{u}^p(x,\omega), \tag{53}$$

where J_0 is the Bessel function of order zero of the first class and N_0 is the Bessel function of order zero of the second class, also known as Neumann function of order zero. The particular solution $\hat{u}^p(x,\omega)$ is given by

$$\hat{u}^p = \frac{B}{k^2} = \frac{1}{i\omega\rho}\,\frac{d\hat{p}}{dx}, \tag{54}$$

and the general solution for $\hat{u}(x,r,\omega)$ is

$$\hat{u}(x,r,\omega) = aJ_0(kr) + bN_0(kr) + \frac{1}{i\omega\rho}\,\frac{d\hat{p}(x,\omega)}{dx}. \tag{55}$$

In order to determine the values of a and b we impose the following boundary conditions: the axial velocity, u, has to be finite at $r = 0$, and zero at the average radius, R_0. This gives Eq. (1) that allows for the computation of velocity profiles. K_L is a local dynamic permeability in frequency domain given by Eq. (2). Inverse Fourier transformation of Eq. (1) allows one to obtain the velocity profiles $u(x,r,t)$ in time domain. Averaging Eq. (1) over the cross sectional area gives a generalized Darcy's law in frequency domain, namely,

$$\hat{U}(x,\omega) = -\frac{K(\omega)}{\eta}\,\frac{\partial\hat{p}(x,\omega)}{\partial x}, \tag{56}$$

where $\hat{U}(x,\omega)$ is the axial velocity averaged over the average cross-sectional area A_0. The dynamic permeability, $K(\omega)$, is simply the average of the local dynamic permeability over the average cross-sectional area and is given by Eq. (4). The x-dependence of $\hat{U}(x,\omega)$ comes from the pressure gradient. Equation (3) follows from Eq. (56) by assuming that the flow is approximately $Q(x,t) \approx A_0U(x,t)$. The approximation of the area by its average A_0 is necessary in order to keep a linear relation between flow and pressure gradient in frequency domain.

The fluid velocity $\mathbf{v} = u(x,r,t)\hat{\imath} + v(x,r,t)\hat{r}$ satisfies the continuity equation

$$\frac{\partial \rho}{\partial t} + \nabla \cdot (\rho \mathbf{v}) = 0. \tag{57}$$

For incompressible fluids in cylindrical coordinates, this one is given by

$$\frac{\partial u}{\partial x} + \frac{1}{r}\frac{\partial (rv)}{\partial r} = 0. \tag{58}$$

Averaging this equation over the mean cross-sectional area gives

$$\frac{\partial U}{\partial x} + \frac{2\pi}{A_0} R_0 v_{r=R_0} = 0, \tag{59}$$

where $U(x,t)$ is the axial velocity averaged over the mean cross-sectional area. We consider that the fluid and wall velocities are equal at the average radius, *i.e.* $v_{r=R_0} = \frac{\partial R}{\partial t}\big|_{R_0}$, which leads to

$$\frac{\partial U}{\partial x} + \frac{2\pi}{A_0} R_0 \frac{\partial R}{\partial t}\bigg|_{R_0} = 0 \tag{60}$$

and, in terms of the flow $Q(x,t) = A_0 U(x,t)$, it becomes

$$\frac{\partial Q}{\partial x} + 2\pi R_0 \frac{\partial R}{\partial t}\bigg|_{R_0} = 0. \tag{61}$$

A relationship between P and R is required to write the local radius of the vessel in terms of the local blood pressure. Here we consider a relationship between the pressure and the elastic deformation of the tube, ΔR,[22,31]

$$p - p_{\text{ext}} = \frac{Eh}{1-\nu^2}\frac{\Delta R}{R_0^2}, \tag{62}$$

where $p - p_{\text{ext}}$ is the transmural pressure, E is the Young modulus, h is the vessel thickness, and ν the Poisson ratio, that we take as $\nu = 1/2$ (*i.e.* we assume the arterial wall to be an incompressible material). Around the radius at diastole, R_{d},

this can be approximated as

$$p - p_{\rm d} = \frac{4}{3} Eh \frac{R - R_{\rm d}}{R_{\rm d}^2}. \tag{63}$$

where $p_{\rm d}$ is the pressure at diastole. This type of 'tube law' has been extensively used in the literature.[3–5, 8, 11, 20, 26, 30, 33, 35, 42–44, 53, 55]

We take the time derivative of Eq.(63) in order to find an expression for the time derivative of the radius in terms of the time derivative of the pressure to be used in Eq. (61). We evaluate it at the average radius, R_0, and obtain

$$\left.\frac{\partial R}{\partial t}\right|_{R_0} = \left.\frac{3R_d^2}{4Eh}\frac{\partial p}{\partial t}\right|_{R_0} = \frac{3R_d^2}{4Eh}\frac{\partial p}{\partial t}. \tag{64}$$

Equations (61) and (64) give equation Eq. (5), in frequency domain, with $C = \frac{3\pi R_0 R_d^2}{2Eh}$.

Appendix II. Full aorta model

This appendix describes the analytical solution for the full-aorta model, which consists of 20 vessels representing the aorta and its first generation of larger branches. At the inlet of the ascending aorta, the flow rate measured *in vivo* was prescribed as the inflow boundary condition, $Q_{\rm in}(t)$. Terminal vessels were coupled to three-element lumped parameter models simulating blood flow and pressure in downstream vessels. Following the notation of Fig. 5, node 1 is of Type I, nodes 2, 3, 5, 6, 7, 8, 9, and 10 are of Type II, node 4 is of Type III, and nodes 11, 12, 13, 14, 15, 16, 17, 18, 19 and 20 are of Type IV. According to Eqs. (29), (30), (31) and (32), the system of equations for the pressures at the nodes, in matrix form and in terms of the functions κ_1^i, κ_2^i and κ_3^i defined in Eq. (28), is given by: $\hat{\mathbf{p}} = \mathbf{K}^{-1}\hat{\mathbf{Q}}$. Here $\hat{\mathbf{p}}$ is the 20-element vector for the pressures at the nodes, $\hat{\mathbf{Q}}$ is the vector of the inflow boundary conditions whose sole non-zero element is the first one and is given by $-\frac{\hat{Q}_{in}^1}{\cos(k_c^1 l^1)}$, and $\mathbf{K}^{-1}$ is the inverse matrix of $\mathbf{K}$, which is a response function of the system. $\mathbf{K}$ is given by:

$$\mathbf{K} = \begin{pmatrix}
a & \kappa_2^2 & 0 & 0 & 0 & 0 & 0 & 0 & 0 & 0 & \kappa_2^{11} & 0 & 0 & 0 & 0 & 0 & 0 & 0 & 0 & 0 \\
\kappa_2^2 & b & \kappa_2^3 & 0 & 0 & 0 & 0 & 0 & 0 & 0 & 0 & \kappa_2^{12} & 0 & 0 & 0 & 0 & 0 & 0 & 0 & 0 \\
0 & \kappa_2^3 & c & \kappa_2^4 & 0 & 0 & 0 & 0 & 0 & 0 & 0 & 0 & \kappa_2^{13} & 0 & 0 & 0 & 0 & 0 & 0 & 0 \\
0 & 0 & \kappa_2^4 & d & \kappa_2^5 & 0 & 0 & 0 & 0 & 0 & 0 & 0 & 0 & 0 & 0 & 0 & 0 & 0 & 0 & 0 \\
0 & 0 & 0 & \kappa_2^5 & e & \kappa_2^6 & 0 & 0 & 0 & 0 & 0 & 0 & 0 & \kappa_2^{14} & 0 & 0 & 0 & 0 & 0 & 0 \\
0 & 0 & 0 & 0 & \kappa_2^6 & f & \kappa_2^7 & 0 & 0 & 0 & 0 & 0 & 0 & 0 & \kappa_2^{15} & 0 & 0 & 0 & 0 & 0 \\
0 & 0 & 0 & 0 & 0 & \kappa_2^7 & g & \kappa_2^8 & 0 & 0 & 0 & 0 & 0 & 0 & 0 & \kappa_2^{16} & 0 & 0 & 0 & 0 \\
0 & 0 & 0 & 0 & 0 & 0 & \kappa_2^8 & h & \kappa_2^9 & 0 & 0 & 0 & 0 & 0 & 0 & 0 & \kappa_2^{17} & 0 & 0 & 0 \\
0 & 0 & 0 & 0 & 0 & 0 & 0 & \kappa_2^9 & j & \kappa_2^{10} & 0 & 0 & 0 & 0 & 0 & 0 & 0 & \kappa_2^{18} & 0 & 0 \\
0 & 0 & 0 & 0 & 0 & 0 & 0 & 0 & \kappa_2^{10} & k & 0 & 0 & 0 & 0 & 0 & 0 & 0 & 0 & \kappa_2^{19} & \kappa_2^{20} \\
\kappa_2^{11} & 0 & 0 & 0 & 0 & 0 & 0 & 0 & 0 & 0 & l & 0 & 0 & 0 & 0 & 0 & 0 & 0 & 0 & 0 \\
0 & \kappa_2^{12} & 0 & 0 & 0 & 0 & 0 & 0 & 0 & 0 & 0 & m & 0 & 0 & 0 & 0 & 0 & 0 & 0 & 0 \\
0 & 0 & \kappa_2^{13} & 0 & 0 & 0 & 0 & 0 & 0 & 0 & 0 & 0 & n & 0 & 0 & 0 & 0 & 0 & 0 & 0 \\
0 & 0 & 0 & 0 & \kappa_2^{14} & 0 & 0 & 0 & 0 & 0 & 0 & 0 & 0 & p & 0 & 0 & 0 & 0 & 0 & 0 \\
0 & 0 & 0 & 0 & 0 & \kappa_2^{15} & 0 & 0 & 0 & 0 & 0 & 0 & 0 & 0 & q & 0 & 0 & 0 & 0 & 0 \\
0 & 0 & 0 & 0 & 0 & 0 & \kappa_2^{16} & 0 & 0 & 0 & 0 & 0 & 0 & 0 & 0 & r & 0 & 0 & 0 & 0 \\
0 & 0 & 0 & 0 & 0 & 0 & 0 & \kappa_2^{17} & 0 & 0 & 0 & 0 & 0 & 0 & 0 & 0 & s & 0 & 0 & 0 \\
0 & 0 & 0 & 0 & 0 & 0 & 0 & 0 & \kappa_2^{18} & 0 & 0 & 0 & 0 & 0 & 0 & 0 & 0 & t & 0 & 0 \\
0 & 0 & 0 & 0 & 0 & 0 & 0 & 0 & 0 & \kappa_2^{19} & 0 & 0 & 0 & 0 & 0 & 0 & 0 & 0 & u & 0 \\
0 & 0 & 0 & 0 & 0 & 0 & 0 & 0 & 0 & \kappa_2^{20} & 0 & 0 & 0 & 0 & 0 & 0 & 0 & 0 & 0 & v
\end{pmatrix},$$

where

$$\begin{aligned}
a &= \kappa_3^1 - \kappa_1^2 - \kappa_1^{11}, & f &= -\kappa_1^6 - \kappa_1^7 - \kappa_1^{15}, & l &= -\kappa_1^{11} - \tfrac{1}{z_{11}}, & r &= -\kappa_1^{16} - \tfrac{1}{z_{16}}, \\
b &= -\kappa_1^2 - \kappa_1^3 - \kappa_1^{12}, & g &= -\kappa_1^7 - \kappa_1^8 - \kappa_1^{16}, & m &= -\kappa_1^{12} - \tfrac{1}{z_{12}}, & s &= -\kappa_1^{17} - \tfrac{1}{z_{17}}, \\
c &= -\kappa_1^3 - \kappa_1^4 - \kappa_1^{13}, & h &= -\kappa_1^8 - \kappa_1^9 - \kappa_1^{17}, & n &= -\kappa_1^{13} - \tfrac{1}{z_{13}}, & t &= -\kappa_1^{18} - \tfrac{1}{z_{18}}, \\
d &= -\kappa_1^4 - \kappa_1^5, & j &= -\kappa_1^9 - \kappa_1^{10} - \kappa_1^{18}, & p &= -\kappa_1^{14} - \tfrac{1}{z_{14}}, & u &= -\kappa_1^{19} - \tfrac{1}{z_{19}}, \\
e &= -\kappa_1^5 - \kappa_1^6 - \kappa_1^{14}, & k &= -\kappa_1^{10} - \kappa_1^{19} - \kappa_1^{20}, & q &= -\kappa_1^{15} - \tfrac{1}{z_{15}}, & v &= -\kappa_1^{20} - \tfrac{1}{z_{20}}.
\end{aligned}$$

Inversion of the matrix $\mathbf{K}$ was done symbolically using Mathematica, which took less than a second on a standard laptop. However, the text length required to explicitly write $\mathbf{K}^{-1}$ and the pressures at the nodes is excessively large to show it in an Appendix. Once the pressures at the nodes were obtained, analytical ex-

pressions for pressure, the flow and velocity profiles in each vessel were calculated using Eqs. (14), (15), and (16) for vessel 1, and Eqs. (8), (10), and (12) for the rest of the vessels. For instance, for the first aortic segment, the pressure at the first node, $\hat{p}^{[1]}$, is necessary in Eqs (14), (15), and (16) where $\hat{p}_o = \hat{p}^{[1]}$. This one is given by:

$$\hat{p}^{[1]} = -\frac{n\ \kappa_2^3\ \mathcal{F}1\ \hat{Q}_{\text{in}}^1}{\kappa_2^2\ \kappa_2^{13}\cos(k_c^1 l^1)} - \frac{B\ \hat{Q}_{\text{in}}^1}{\kappa_2^2\ \kappa_2^{11}\kappa_2^{12}\cos(k_c^1 l^1)}\left[\frac{p\ \kappa_2^4\ \kappa_2^5\ \kappa_2^{12}\ \mathcal{F}2}{d\ m\ \kappa_2^3\ \kappa_2^{14}} - \frac{\mathcal{F}1\ \text{T9}}{d\ m\ \kappa_2^3\ \left(\kappa_2^{13}\right)^2}\right], \tag{65}$$

with

$$\mathcal{F}1 = \frac{\mathcal{F}2\ \text{T7}}{n\ \kappa_2^4\ \kappa_2^5\ \kappa_2^{14}} + \frac{d\ q\ \kappa_2^6\ \kappa_2^{13}\ \mathcal{F}3}{n\ \kappa_2^4\ \kappa_2^5\ \kappa_2^{15}}, \tag{66}$$

$$\mathcal{F}2 = -\left(\frac{F\ \mathcal{F}3}{p\ \kappa_2^6\ \kappa_2^{15}} + \frac{r\ \kappa_2^7\ \kappa_2^{14}\ \mathcal{F}4}{p\ \kappa_2^6\ \kappa_2^{16}}\right), \tag{67}$$

$$\mathcal{F}3 = -\left(\frac{G\ \mathcal{F}4}{q\ \kappa_2^7\ \kappa_2^{16}} + \frac{s\ \kappa_2^8\ \kappa_2^{15}\ \mathcal{F}5}{q\ \kappa_2^7\ \kappa_2^{17}}\right), \tag{68}$$

$$\mathcal{F}4 = -\left(\frac{H\mathcal{F}5}{r\ \kappa_2^8\ \kappa_2^{17}} + \frac{t\ \kappa_2^9\ \kappa_2^{16}\mathcal{F}6}{r\ \kappa_2^8\ \kappa_2^{18}}\right), \tag{69}$$

$$\mathcal{F}5 = \frac{\text{N3}}{\mathcal{M}} - \frac{J\mathcal{F}6}{s\ \kappa_2^9\ \kappa_2^{18}}, \tag{70}$$

$$\mathcal{F}6 = \frac{\text{N1} - \text{N2}}{\mathcal{M}}. \tag{71}$$

These quantities contain another set of definitions given by:

$$\text{N1} = d\ l\ m\ n\ p\ q\ r\ s\ u\ \kappa_2^2\ \kappa_2^3\ \kappa_2^4\ \kappa_2^5\ \kappa_2^6\ \kappa_2^7\ \kappa_2^8\ \kappa_2^9\ \kappa_2^{11}\left(\kappa_2^{12}\ \kappa_2^{14}\ \kappa_2^{15}\ \kappa_2^{16}\ \kappa_2^{17}\ \kappa_2^{18}\ \kappa_2^{20}\right)^2\left(\kappa_2^{13}\right)^3 K, \tag{72}$$

$$\text{N2} = d\ l\ m\ n\ p\ q\ r\ s\ v\ \kappa_2^2\ \kappa_2^3\ \kappa_2^4\ \kappa_2^5\ \kappa_2^6\ \kappa_2^7\ \kappa_2^8\ \kappa_2^9\ \kappa_2^{11}\left(\kappa_2^{12}\ \kappa_2^{14}\ \kappa_2^{15}\ \kappa_2^{16}\ \kappa_2^{17}\ \kappa_2^{19}\ \kappa_2^{20}\right)^2\left(\kappa_2^{13}\ \kappa_2^{18}\right)^3, \tag{73}$$

$$\text{N3} = d\ l\ m\ n\ p\ q\ r\ t\ u\ v\ \kappa_2^2\ \kappa_2^3\ \kappa_2^4\ \kappa_2^5\ \kappa_2^6\ \kappa_2^7\ \kappa_2^8\ \kappa_2^{11}\left(\kappa_2^{10}\ \kappa_2^{12}\ \kappa_2^{14}\ \kappa_2^{15}\ \kappa_2^{16}\ \kappa_2^{18}\ \kappa_2^{20}\right)^2\left(\kappa_2^{13}\ \kappa_2^{17}\right)^3, \tag{74}$$

$$\mathcal{M} = -v\ \kappa_2^{18}\kappa_2^{20}\left(\kappa_2^{19}\right)^2\text{T1} + u\ \kappa_2^{20}\left(K\ \text{T1} - t\ v\ \kappa_2^{17}\ \kappa_2^{18}\ \kappa_2^{20}\left(\kappa_2^{10}\right)^2\text{T2}\right), \tag{75}$$

$$\text{T1} = \kappa_2^{20} J\ \text{T2} - s\ t\ \kappa_2^{16}\ \kappa_2^{17}\kappa_2^{18}\kappa_2^{20}\left(\kappa_2^9\right)^2\text{T3}, \tag{76}$$

$$\mathrm{T2} = \kappa_2^{18} H\ \mathrm{T3} - r\ s\ \kappa_2^{15}\ \kappa_2^{16}\ \kappa_2^{17}\kappa_2^{18}\left(\kappa_2^{8}\right)^2\ \mathrm{T4}, \tag{77}$$

$$\mathrm{T3} = \kappa_2^{17}\ G\ \mathrm{T4} - q\ r\ \kappa_2^{14}\ \kappa_2^{15}\ \kappa_2^{16}\kappa_2^{17}\left(\kappa_2^{7}\right)^2\ \mathrm{T5}, \tag{78}$$

$$\mathrm{T4} = \kappa_2^{16}\ F\ \mathrm{T5} - d\ p\ q\ \kappa_2^{13}\ \kappa_2^{14}\ \kappa_2^{15}\kappa_2^{16}\left(\kappa_2^{6}\right)^2\ \mathrm{T6}, \tag{79}$$

$$\mathrm{T5} = \kappa_2^{15}\ \mathrm{T6}\ \mathrm{T7} + n\ p\ \kappa_2^{12}\ \kappa_2^{14}\ \kappa_2^{15}\left(\kappa_2^{4}\ \kappa_2^{5}\ \kappa_2^{13}\right)^2\ \mathrm{T8}, \tag{80}$$

$$\mathrm{T6} = d\ m\ n\ \kappa_2^{11}\ \kappa_2^{14}\left(\kappa_2^{3}\ \kappa_2^{12}\ \kappa_2^{13}\right)^2 A - \kappa_2^{14}\ \mathrm{T8}\ \mathrm{T9}, \tag{81}$$

$$\mathrm{T7} = p\ D - d\ \kappa_2^{13}\left(\kappa_2^{14}\right)^2, \tag{82}$$

$$\mathrm{T8} = \kappa_2^{12}\ \kappa_2^{13} A\ B - l\ m\ \kappa_2^{11}\ \kappa_2^{12}\ \kappa_2^{13}\left(\kappa_2^{2}\right)^2, \tag{83}$$

$$\mathrm{T9} = d\ C\ \kappa_2^{13} - n\ \kappa_2^{12}\kappa_2^{13}\left(\kappa_2^{4}\right)^2, \tag{84}$$

that in turn contain a third set of definitions given by:

$$A = a\ l - \left(\kappa_2^{11}\right)^2, \tag{85}$$

$$B = b\ m\ \kappa_2^{11} - \kappa_2^{11}\left(\kappa_2^{12}\right)^2, \tag{86}$$

$$C = c\ n\ \kappa_2^{12} - \kappa_2^{12}\left(\kappa_2^{13}\right)^2, \tag{87}$$

$$D = d\ e\ \kappa_2^{13} - \kappa_2^{13}\left(\kappa_2^{5}\right)^2, \tag{88}$$

$$F = f\ q\ \kappa_2^{14} - \kappa_2^{14}\left(\kappa_2^{15}\right)^2, \tag{89}$$

$$G = g\ r\ \kappa_2^{15} - \kappa_2^{15}\left(\kappa_2^{16}\right)^2, \tag{90}$$

$$H = h\ s\ \kappa_2^{16} - \kappa_2^{16}\left(\kappa_2^{17}\right)^2, \tag{91}$$

$$J = j\ t\ \kappa_2^{17} - \kappa_2^{17}\left(\kappa_2^{18}\right)^2, \tag{92}$$

$$K = k\ v\ \kappa_2^{18} - \kappa_2^{18}\left(\kappa_2^{20}\right)^2. \tag{93}$$

Appendix III. Error calculations

For the test cases presented in Sections 3.1 to 3.4, the numerical solutions of pressure (p), pressure difference between inlet and outlet (Δp), volumetric flow rate (Q), and change in radius from diastole (Δr) given by the analytical GDEM were compared with corresponding values provided by computational 1-D and 3-D formulations. We used the following relative error metrics for p and Q:

$$\mathcal{E}_p^{RMS} = \sqrt{\frac{1}{n}\sum_{i=1}^{n}\left(\frac{p_i^{\mathrm{GDEM}} - \mathscr{P}_i}{\mathscr{P}_i}\right)^2}, \quad \mathcal{E}_Q^{RMS} = \sqrt{\frac{1}{n}\sum_{i=1}^{n}\left(\frac{Q_i^{\mathrm{GDEM}} - \mathscr{Q}_i}{\max_j(\mathscr{Q}_j)}\right)^2}, \tag{94}$$

$$\mathcal{E}_p^{MAX} = \max_i\left|\frac{p_i^{\mathrm{GDEM}} - \mathscr{P}_i}{\mathscr{P}_i}\right|, \qquad \mathcal{E}_Q^{MAX} = \max_i\left|\frac{Q_i^{\mathrm{GDEM}} - \mathscr{Q}_i}{\max_j(\mathscr{Q}_j)}\right|, \tag{95}$$

$$\mathcal{E}_p^{SYS} = \frac{\max(p^{\mathrm{GDEM}}) - \max(\mathscr{P})}{\max(\mathscr{P})}, \qquad \mathcal{E}_Q^{SYS} = \frac{\max(Q^{\mathrm{GDEM}}) - \max(\mathscr{Q})}{\max(\mathscr{Q})}, \tag{96}$$

$$\mathcal{E}_p^{DIAS} = \frac{\min(p^{\mathrm{GDEM}}) - \min(\mathscr{P})}{\min(\mathscr{P})}, \qquad \mathcal{E}_Q^{DIAS} = \frac{\min(Q^{\mathrm{GDEM}}) - \min(\mathscr{Q})}{\max(\mathscr{Q})}, \tag{97}$$

where p_i^{GDEM} and Q_i^{GDEM} are the results obtained using the analytical GDEM at a given spatial location and time point i ($i = 1, \ldots, n$). At the same spatial location and time point i, $\mathscr{P}_i$ and $\mathscr{Q}_i$ are either the pressure and flow given by the linear 1-D model or the cross-sectional averaged pressure and flow calculated from the 3-D model. The number of time points n was determined by the 3-D solution. $\mathcal{E}_p^{RMS}$ and $\mathcal{E}_Q^{RMS}$ are the root mean square relative errors for pressure and flow; $\mathcal{E}_p^{MAX}$ and $\mathcal{E}_Q^{MAX}$ are the maximum relative errors in pressure and flow; $\mathcal{E}_p^{SYS}$ and $\mathcal{E}_Q^{SYS}$ are the errors in systolic pressure and flow; and $\mathcal{E}_p^{DIAS}$ and $\mathcal{E}_Q^{DIAS}$ are the errors in diastolic pressure and flow, respectively. Flow errors were normalized by the maximal flow over the cardiac cycle to avoid division by small values of the flow. For the quantities Δp and Δr we used the same metrics as for the flow rate. All error metrics were calculated over a single cardiac cycle, using the numerical 1-D and 3-D results in the periodic regime.